IEEE Access
Multidisciplinary | Rapid Review | Open Access Journal

Received April 27, 2019, accepted July 3, 2019, date of publication July 19, 2019, date of current version August 7, 2019.

Digital Object Identifier 10.1109/ACCESS.2019.2930114

Research on Damages Evaluation Method With Multi-Objective Feature Extraction Optimization Scheme for M/OD Impact Risk Assessment

CHUN YIN[1], (Member, IEEE), TING XUE[1], XUEGANG HUANG[2], YU-HUA CHENG[1], SARA DADRAS[3], (Senior Member, IEEE), AND SOODEH DADRAS[3], (Member, IEEE)

[1]School of Automation Engineering, University of Electronic Science and Technology of China, Chengdu 611731, China
[2]Hypervelocity Aerodynamics Institute, China Aerodynamics Research and Development Center, Mianyang 621000, China
[3]Electrical and Computer Engineering Department, Utah State University, Logan, UT 84321, USA

Corresponding author: Xuegang Huang (emei-126@126.com)

This work was supported in part by the National Basic Research Program of China under Grant 61873305, Grant 61671109, and Grant U1830207, and in part by the Sichuan Science and Technology Plan Project under Grant 2018JY0410 and Grant 2019YJ0199.

ABSTRACT As the number of space debris (also called meteoroid/orbital debris-M/OD) increases in recent years, the hypervelocity-impact (HVI) events of M/OD on spacecrafts have become one of the most main risks threatening human activity in space. For the automatical M/OD risk assessment, some effective nondestructive testing (NDT) methods are critical to realizing the evaluation of the HVI damages. In this paper, a novel HVI damage evaluation method based on the active infrared thermal wave image detection technology with multi-objective feature extraction optimization (MO-FEO) is proposed to achieve the quantitative evaluation of M/OD HVI damages. For the precise selection of representative temperature point in thermal infrared image data, the proposed MO-FEO method has the advantage not only of considering the difference among temperature points in different thermal temperature categories but also considering the correlation among temperature points of each thermal temperature category. The multi-objective feature extraction problem decomposed by Tchebycheff aggregation is used to seek the representative temperature points through an evolution process brought the selection pressure and fitness value. In addition to the MO-FEO frame, the variable step search and classification of temperature points are also implemented in the HVI damage evaluation strategy to improve efficiency. Some experimental results of infrared detection for the real M/OD HVI test articles are proposed to illustrate the effectiveness of the proposed method.

INDEX TERMS M/OD hypervelocity impact, impact risk assessment, damage evaluation, multi-objective optimization, evolution analysis.

I. INTRODUCTION

With the increasing human activities in space, more and more spacecrafts have been sent into the earth's orbit or deep space [1], [2]. Accidental and intended at times, breakups or explosions of the spacecrafts have created a lot of fragments in varying shapes and sizes over the years, which leads to the deteriorated earth's orbital-debris-environment [3], [4]. Besides the man-made space junk, the meteoroid is another natural-source of the space debris, which includes asteroidal or cometary debris in orbit around the Sun. Nowadays, the M/OD HVI risk has turned into a major threat to human activities in space [5], [6], which has brought some evident negative effects to the spacecrafts in space, such as impact craters caused by the HVI of small M/OD as shown in Figure 1. Owing to the unpredictability of M/OD impact events, the impact conditions (such as impact velocity/angle, debris size/quantity) are random, causing the consequential damages are very complicated to be detected [7]–[9]. Hence, the automatical M/OD risk assessment is critical for various spacecraft, and the HVI damage evaluation based on some effective NDT technologies is an important component of it.

The infrared thermal wave image detection technology can acquire surface/subsurface structural damage information of the test articles by utilizing the thermal excitation method and measuring change of infrared radiant temperature

The associate editor coordinating the review of this manuscript and approving it for publication was Chee Keong Kwoh.

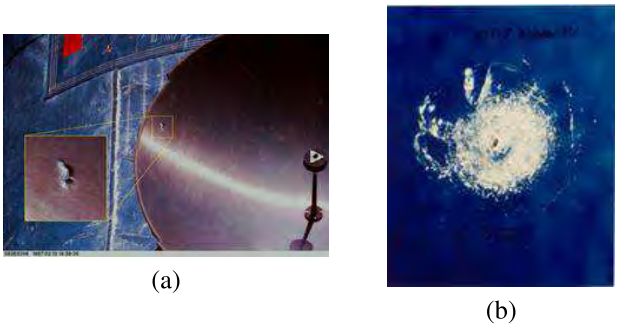

(a) (b)

FIGURE 1. M/OD impact crater on spacecraft's scuttle [5].

field of material surface [10]–[13]. Infrared thermal image sequence contains mass valid data and strong noise interference, it is very important to extract the key defect feature from image sequence for a better detection results. Over the last few decades, some image processing algorithms have been proposed by researchers to investigate the temperature field change caused by defect and distinguish the defect area from the background area. To extract the thermal feature, Fourier Transform methods can transform transient temperature responses (TTRs) of each frame in time domain to ones in frequency domain, however, the frequency selection still rely on personal experience [14], [15]. Principal component analysis (PCA) and independent component analysis (ICA) have also been used to separate the damage's feature information from the infrared image sequence through the space-time information mining [16]–[18]. Some related studies [16] have demonstrated that ICA is able to realize the feature extraction more effectively than PCA does. In addition, some other images processing algorithms based on representative temperature points extraction proposed in [19], [20] can achieve higher efficiency than ICA method. For the extraction of representative temperature points, the between-class distance decision scheme, which mainly considering the difference calculation of different categories, has been applied in [19], [20]. However, the correlation between the representative temperature point and the other temperature points in same category have not yet been investigated in these relevant literatures, so that the selected representative temperature points are less representative of their own categories. Hence, both the difference and the similarity of temperature points in infrared image sequence data should be adequately considered in the selection of the representative temperature point in damage evaluation.

Actually, the problem about multiple contradictory objectives is very common in some other practical problems, such as hexa-Rotor [21], [22], interferometric aperture synthesis [23], and complex network clustering [24], [25]. In dealing with these multi-objective problems, the conventional weighting method has many limitations in computing efficiency and accuracy due to the difficulty of obtaining exact weight coefficient, so it can not be regarded as an effective solution to our problem. But it is worth reminding that, the Pareto solution under the multi-objective evolutionary algorithm obtains a compromise between the multiple contradictory sub-objectives [26]–[29]. When considering how to select representative feature points, the double difficulties of establishing multi-objective problems as well as searching candidate representative temperature points should be solved simultaneously, which would be caused by high-dimensional data and high-dimensional target numbers.

Based on the above purposes, a defect feature extraction and quantitative evaluation method with the MO-FEO scheme based on infrared image data is proposed to automatically detect and evaluate the HVI damages of M/OD. The multi-objective optimization method plays an important role in the infrared image feature extraction algorithm, which can achieve multi-performance considerations including difference and similarity in representative feature selection. The solutions of the multi-objective feature extraction problems are used to generate Pareto front (PF) and select the representative temperature point, and thereby the quantitative damage evaluation and efficient risk assessment are realized in M/OD HVI event. Moreover, the variable step search and classification of temperature points are also implemented in the HVI damage evaluation strategy to improve the efficiency. Experimental results based on the actual infrared image sequences data of M/OD HVI test articles are provided to demonstrate the validity and advantage of the proposed method.

II. MULTI-OBJECTIVE FEATURE EXTRACTION OPTIMIZATION ALGORITHM

Different sized space debris may result in very big different impact damages to spacecraft [5], [6]. M/OD objects larger than about 10 cm in LEO and 1 m in GEO are often considered as the large-size space debris, which causes some serious structural failure of spacecraft, but the large-size M/OD can be monitored and cataloged by optical sensor systems or ground-based radar, so the impact risk can be effectively reduced by posture adjustment and orbit modulation of spacecraft. However, for small-size M/OD (usually centimeter-scale or below) which cannot be monitored and cataloged due to its smaller size and enormous amount, the risk and hazard of hypervelocity impacts will be more serious than that of large-size M/OD HVI. Accordingly, the detection and evaluation of HVI damage are necessary and vital for the impact risk assessment. For instance, a conventional hypervelocity impact of micro-scale M/OD on the thermal protection system can generate the surface/internal damage (i.e. crack, crater, delamination/spalling) of thermal protection materials, which may cause the disintegration and explosion of spacecrafts during their re-entry flights in earth's atmosphere. More seriously, the amount of micro M/OD on earthąs orbit is immense, so the collision probability and potential hazard are very high. Hence, it is necessary first to evaluate the M/OD HVI damages by using some available NDT technologies, which is very important for the M/OD risk prediction and the performance evaluation of various spacecrafts.

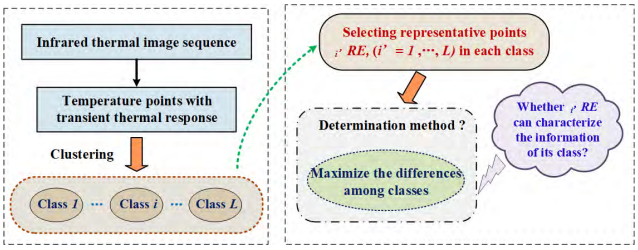

FIGURE 2. The selection of temperature points in [19], [20].

Infrared thermography testing technology is a kind of effective nondestructive detection means, which can detect surface/subsurface damages of various aerospace materials based on the temperature field change of the test articles captured by infrared camera. For the purpose of reducing the data redundancy, enhancing the detection image quality, and improving the detection efficiency, it is necessary to extract the defect feature information from the infrared thermal image sequence. As shown in Figure 2, consulting our previous research works [19], [20], each pixel in the image can be regarded as a temperature point with TTR varying with time. A representative temperature point ${}_{i'}RE$ is picked from each category based on a certain determination method to acquire feature extraction, in which case the determination method is the core content of the selection of a more representative point ${}_{i'}RE$.

The determination method in [19], [20] focuses mainly on the difference performance among different categories. Specifically, ${}_{i'}RE$ is picked based on the following formula:

$$ {}_{i'}RE = \arg\limits_{{}_{i'}\mathcal{X}} \left(\max\limits_{{}_{i'}\mathcal{X}\in{}_{i'}\Theta} \left\{ \sum_{\substack{j'=1 \\ j'\neq i'}}^{L} \left\| {}_{i'}\mathcal{X} - {}_{j'}Center \right\| \right\} \right) \tag{1} $$

in which ${}_{i'}RE$ owns the greatest difference with the other categories, ${}_{i'}\Theta$ denotes the i'-th category, ${}_{i'}\mathcal{X}$ expresses TTR in the i'-th category, ${}_{j'}Center$ is TTR of the cluster center of the j'-th $\left(j' = 1, \cdots, L, j' \neq i'\right)$ category. The selection of ${}_{i'}RE$ based on difference is a feasible method, but the above method cannot determine the correlation between the representative temperature points and their corresponding categories. According to our new research result, it found that ${}_{i'}RE$ could be an edge point that has a weak correlation with other temperature points in the same category, then the selected temperature point may be not sufficient to characterize the category.

Remark 1: To investigate the characterization performance of ${}_{i'}RE$, it should study whether ${}_{i'}RE$ has a great correlation with similar temperature points. ${}_{i'}RE, i' = 1, 2, 3$ derived by the difference method [19], [20] are displayed in Figure 3. Moreover, the related data-information of each category is listed in Table 1. Table 2 shows further the correlation and difference values among three representative temperature points and cluster center, respectively. Obviously,

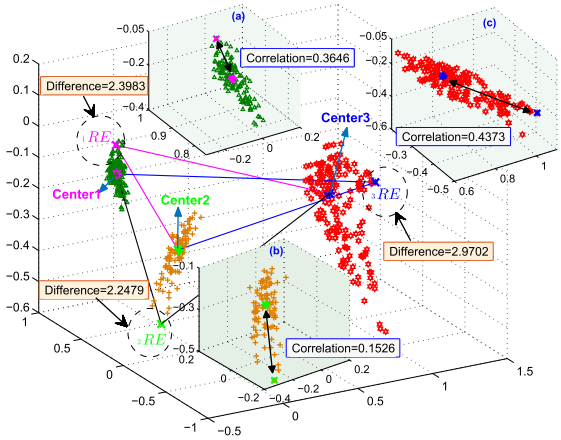

FIGURE 3. Representative temperature points selected by the difference method.

TABLE 1. Related data information for each category.

	Points	Center	Representative points
Category 1	163	(-0.0864,0.8109,-0.1615)	(-0.0503,0.9283,-0.1182)
Category 2	101	(-0.1117,0.0483,-0.2728)	(-0.3900,0.2523,-0.4344)
Category 3	139	(0.4153,-0.0257,0.2240)	(0.4410,-0.1411,0.2079)

TABLE 2. Correlation and difference values of the representative temperature points selected by the difference method.

	Center 1	*Center* 2	*Center* 3	Correlation	Difference
${}_1RE$	**0.3646**	0.9106	1.4877	0.3646	2.3983
${}_2RE$	1.1389	**0.1526**	1.1090	0.1526	2.2479
${}_3RE$	1.7682	1.2020	**0.4373**	0.4373	2.9702

the correlation between ${}_{i'}RE$ and Center$i'(i' = 1, 2, 3)$ is small, so that the selected points cannot be sufficient to characterize their corresponding category.

Hence, the representative temperature points extracted by only considering the difference calculation of different categories is insufficient to represent the real characteristic of their own categories. To extract effectively the damage features, it is hoped that the selected representative temperature points ${}_iRE$ can not only satisfy the biggest difference with temperature points of other categories, but also ensure the strongest correlation with similar temperature points of their own categories. Actually, It is almost impossible to achieve both goals above-mentioned at the same time, so it is necessary to achieves a compromise between these two goals. The proposed algorithm of this paper focuses on solving the problem that the selected point may be weakly correlated with TTR of other similar temperature points while guaranteeing the sufficient difference.

A. MULTI-OBJECTIVE FEATURE EXTRACTION OPTIMIZATION ALGORITHM FRAMEWORK

In this paper, we investigate mainly the seeking problem of the representative temperature point for multi-performance consideration of difference and correlation. When selecting the representative temperature point ${}_{i'}RE$ in the i'-

th$(i' = 1, ..., L)$ category, the seeking problem can be written in the following:

$$\begin{aligned} &minimize \ \ {}_{i'}F\left({}_{i'}\mathcal{X}\right) = \left({}_{i'}f_1\left({}_{i'}\mathcal{X}\right), \cdots, {}_{i'}f_L\left({}_{i'}\mathcal{X}\right)\right)^T, \\ &subject \ \ to \ \ {}_{i'}\mathcal{X} \in {}_{i'}\Theta, \quad i' = 1, ..., L, \end{aligned} \tag{2}$$

in which ${}_{i'}\Theta$ is determined by the T-time dimension TTRs in the i'-th category. L denotes the clustering number. ${}_{i'}f_i\left({}_{i'}\mathcal{X}\right), i = 1, \cdots, L$ can be stated as follows: ${}_{i'}f_1\left({}_{i'}\mathcal{X}\right) = \sqrt{\sum_{\rho=1}^{T}\left({}_{i'}x_\rho - {}_{i'}Center_\rho\right)^2}$, $\underset{i=2,...,L}{{}_{i'}f_i}\left({}_{i'}\mathcal{X}\right) = -\sqrt{\sum_{\rho=1}^{T}\left({}_{i'}x_\rho - {}_{j'}Center_\rho\right)^2}$, in which ${}_{i'}\mathcal{X} = \left({}_{i'}x_1, \cdots, {}_{i'}x_T\right) \in {}_{i'}\Theta$ is the transient thermal response of a temperature point in the i'-th category; ${}_{i'}Center = \left({}_{i'}Center_1, \cdots, {}_{i'}Center_T\right) \in R^T$, ${}_{j'}Center = \left({}_{j'}Center_1, \cdots, {}_{j'}Center_T\right) \in R^T, j' = 2, \cdots, L, j' \neq i'$.

Several scalar temperature seeking sub-problems after decomposition are built to solve multi-objective feature extraction optimization problem. At each evolution generation κ, the specific MO-FEO algorithm for selecting the representative temperature point ${}_{i'}RE$ in ${}_{i'}\Theta$ is given as follows:

Step a1) The i'-th category involves ${}_{i'}M$ temperature points with T time dimension; the clustering center is a $T \times 1$ vector, marked as ${}_{i'}Center$, which can be derived in Step 2 of Section III.

Step a2) Initialize a group of uniformly distributed weight vectors $\vec{{}_{i'}\omega}^1, \cdots, \vec{{}_{i'}\omega}^{\mathcal{N}_\varrho}$ for the i'-th category. The temperature seeking sub-problem under the Tchebycheff aggregation method [27], [28] can be expressed as follows:

$$\begin{aligned} &\min_{{}_{i'}\mathcal{X} \in {}_{i'}\Theta} g^{tf}\left({}_{i'}\mathcal{X} \left| \vec{{}_{i'}\omega}^j, {}_{i'}r^* \right.\right) \\ &\qquad = \min_{{}_{i'}\mathcal{X} \in {}_{i'}\Omega} \max_{1 \le i \le L} \left\{ {}_{i'}\omega_i^j \left| {}_{i'}f_i\left({}_{i'}\mathcal{X}\right) - {}_{i'}r_i^* \right| \right\}, \end{aligned} \tag{3}$$

where ${}_{i'}r^* = \left({}_{i'}r_1^*, {}_{i'}r_2^*, ..., {}_{i'}r_L^*\right), {}_{i'}r^* \in R^L$, and ${}_{i'}r_j^* = \min\left\{{}_{i'}f_j\left({}_{i'}\mathcal{X}\right) | {}_{i'}\mathcal{X} \in {}_{i'}\Theta\right\}$ is the temperature reference point corresponding to the objective function ${}_{i'}f_j$. $\vec{{}_{i'}\omega}^j = \left({}_{i'}\omega_1^j, \cdots, {}_{i'}\omega_L^j\right)^T, \sum_{i=1}^{L} {}_{i'}\omega_i^j = 1$.

Step a3) Select randomly $\mathcal{N}_\varrho$ temperature points ${}_{i'}\mathcal{X}'^1\left(0\right), \cdots, {}_{i'}\mathcal{X}'^{\mathcal{N}_\varrho}\left(0\right) \in {}_{i'}\Theta$ as initial population. Let the parameter $\kappa = 0$. Then, generate further the initialization temperature points ${}_{i'}\mathcal{X}^1\left(0\right), \cdots, {}_{i'}\mathcal{X}^{\mathcal{N}_\varrho}\left(0\right)$ of the i'-th category by adjusting the sequence of the above points on the basis of the following formula

$${}_{i'}\mathcal{X}^i\left(0\right) = \min_{1 \le j \le \mathcal{N}_\varrho} \left\{ {}_{i'}\mathcal{X}^j\left(0\right) \left| \left\| {}_{i'}\mathcal{X}'^j\left(0\right) - \vec{{}_{i'}\omega}^i \right\|_2 \right. \right\} \tag{4}$$

where $i = 1, \cdots, \mathcal{N}_\varrho$.

Step a4) Set ${}_{i'}NDS\left(0\right) = \emptyset$, that denotes a set stored candidates (i.e. non-dominated solutions) for the representative temperature points. Moreover, initialize the reference point ${}_{i'}r\left(0\right) = \left({}_{i'}r_1\left(0\right), \cdots, {}_{i'}r_L\left(0\right)\right)^T$ where ${}_{i'}r_i\left(0\right) = \min\left\{{}_{i'}f_i\left({}_{i'}\mathcal{X}^1\left(0\right)\right), \cdots, {}_{i'}f_i\left({}_{i'}\mathcal{X}^{\mathcal{N}_\varrho}\left(0\right)\right)\right\}, i = 1, \cdots, L$.

Step a5) Search the η nearest weight vectors by applying the following formula:

$${}_{i'}\Pi^{ij} = \sqrt{\sum_{k=1}^{L}\left({}_{i'}\omega_k^j - {}_{i'}\omega_k^i\right)^2}, \quad j = 1, \cdots, \mathcal{N}_\varrho, \ j \neq i. \tag{5}$$

The index set of η nearest weight vectors of $\vec{{}_{i'}\omega}^i$ is denoted as ${}_{i'}\mathcal{B}\left[i\right] = \left\{i_1, i_2, \cdots, i_\eta\right\}, i = 1, \cdots, \mathcal{N}_\varrho$, therefore, η nearest weight vectors for $\vec{{}_{i'}\omega}^i$ is $\vec{{}_{i'}\omega}^{i_1}, \vec{{}_{i'}\omega}^{i_2}, \cdots, \vec{{}_{i'}\omega}^{i_\eta}$.

Step a6) At the κ-th evolution generation, the following update operations are performed for each weight vector $\vec{{}_{i'}\omega}^i$.

1) Select randomly two index numbers p and q from ${}_{i'}\mathcal{B}\left[i\right]$, and then generate a newly-generated population temperature point ${}_{i'}\mathcal{Y}\left(\kappa\right) = {}_{i'}\mathcal{GP} \times {}_{i'}\mathcal{X}^p\left(\kappa\right) + \left(1 - {}_{i'}\mathcal{GP}\right) \times {}_{i'}\mathcal{X}^q\left(\kappa\right)$ based on ${}_{i'}\mathcal{X}^p\left(\kappa\right)$ and ${}_{i'}\mathcal{X}^q\left(\kappa\right)$, in which ${}_{i'}\mathcal{GP} \in (0, 1)$ denotes a variation threshold.
2) Renew ${}_{i'}r\left(\kappa\right)$: If ${}_{i'}f_j\left({}_{i'}\mathcal{Y}\left(\kappa\right)\right) < {}_{i'}r_j\left(\kappa\right)$, let ${}_{i'}r_j\left(\kappa\right) = {}_{i'}f_j\left({}_{i'}\mathcal{Y}\left(\kappa\right)\right)$ for each $j = 1, 2, \cdots, L$, where ${}_{i'}r_j\left(\kappa\right)$ is the reference point of the function ${}_{i'}f_j$.
3) Renew neighborhood solutions: For each index $j \in {}_{i'}\mathcal{B}\left[i\right]$, if $g^{tf}\left({}_{i'}\mathcal{Y}\left(\kappa\right) \left| \vec{{}_{i'}\omega}^j, {}_{i'}r\left(\kappa\right) \right.\right) \le g^{tf}\left({}_{i'}\mathcal{X}^j\left(t\right) \left| \vec{{}_{i'}\omega}^j, {}_{i'}r\left(\kappa\right) \right.\right)$, let ${}_{i'}\mathcal{X}^j\left(\kappa + 1\right) = {}_{i'}\mathcal{Y}^j\left(\kappa\right)$;
4) Renew ${}_{i'}NDS\left(\kappa\right)$: Replace all solutions dominated by ${}_{i'}F\left({}_{i'}\mathcal{Y}\left(\kappa\right)\right)$ in ${}_{i'}NDS\left(\kappa\right)$ with ${}_{i'}F\left({}_{i'}\mathcal{Y}\left(\kappa\right)\right)$; If no solutions in ${}_{i'}NDS\left(\kappa\right)$ dominate ${}_{i'}F\left({}_{i'}\mathcal{Y}\left(\kappa\right)\right)$, add ${}_{i'}F\left({}_{i'}\mathcal{Y}\left(\kappa\right)\right)$ into ${}_{i'}NDS\left(t\right)$. Then let $i = i + 1$.

Step a7) If $i > \mathcal{N}_\varrho$, let $\kappa = \kappa + 1$; if the stopping criteria isn't achieved, repeat Step a6). Otherwise, then stop and output ${}_{i'}NDS$, and record the number of solutions in ${}_{i'}NDS$ as ${}_{i'}\mathcal{N}_{nds}$.

Step a8) Select the best compromise solution from ${}_{i'}NDS$, $i' \in (1, 2, ..., L)$, that is, determine representative temperature points from L categories:

1) Compute the membership ${}_{i'}\mu_i\left({}_{i'}\mathcal{X}^k\right)$ of the i-th objective function value of the k-th solution in the ${}_{i'}NDS$ according to the formula:

$$\begin{aligned} &{}_{i'}\mu_i\left({}_{i'}\mathcal{X}^k\right) \\ &= \begin{cases} 0, & {}_{i'}f_i\left({}_{i'}\mathcal{X}^k\right) > \max\left({}_{i'}f_i\left({}_{i'}\mathcal{X}^k\right)\right) \\ \dfrac{\min\left({}_{i'}f_i\left({}_{i'}\mathcal{X}^k\right)\right) - {}_{i'}f_i\left({}_{i'}\mathcal{X}^k\right)}{\max\left({}_{i'}f_i\left({}_{i'}\mathcal{X}^k\right)\right) - \min\left({}_{i'}f_i\left({}_{i'}\mathcal{X}^k\right)\right)}, & others \\ 1, {}_{i'}f_i\left({}_{i'}\mathcal{X}^k\right) \le \min\left({}_{i'}f_i\left({}_{i'}\mathcal{X}^k\right)\right) \end{cases} \end{aligned} \tag{6}$$

where ${}_{i'}\mathcal{X}^k \in {}_{i'}NDS, i = 1, \cdots, L, k = 1, \cdots, {}_{i'}\mathcal{N}_{nds}$, $\min\left({}_{i'}f_i\left({}_{i'}\mathcal{X}^k\right)\right)$ and $\max\left({}_{i'}f_i\left({}_{i'}\mathcal{X}^k\right)\right)$ express separately the corresponding minimum and maximum values of the target function.

2) For the k-th solution ${}_{i'}\mathcal{X}^k$ in the ${}_{i'}NDS$, calculate its standardized satisfaction ${}_{i'}\mathcal{U}\left({}_{i'}\mathcal{X}^k\right) = \sum_{i=1}^{L} {}_{i'}\mu_i\left({}_{i'}\mathcal{X}^k\right) / \sum_{k=1}^{{}_{i'}\mathcal{N}_{nds}} \sum_{i=1}^{L} {}_{i'}\mu_i\left({}_{i'}\mathcal{X}^k\right)$.
3) Obtain a compromise optimization solution ${}_{i'}NFCM$ from ${}_{i'}NDS$ by applying the following formula ${}_{i'}NFCM = \left\{{}_{i'}\mathcal{X}^k | \max_{1\le k\le {}_{i'}\mathcal{N}_{nds}} {}_{i'}\mathcal{U}\left({}_{i'}\mathcal{X}^k\right)\right\}$. Then, all of the ${}_{i'}NFCM, i' \in (1, 2, ..., L)$ constitute a $T \times L$ matrix Y, which will be applied in Step 3 of Section III.

It is clear that ${}_{i'}NFCM$ is the selected representative temperature point under the MO-FEO algorithm. Comparing with ${}_{i'}RE$ from (1) in [19], [20], ${}_{i'}NFCM$ is extracted on the basis of multi-performance consideration of difference (i.e. difference with temperature points of other categories) and correlation (i.e. correlation with similar temperature points in the same category). The MO-FEO algorithm can avoid the problem existed in [19], [20], that is, the selected representative temperature point may be weakly correlated with the transient thermal response of other similar temperature points under the premise of ensuring the difference.

B. ANALYSIS OF THE PROPOSED MO-FEO ALGORITHM

In this section, Tchebycheff aggregation method is utilized to approximate PF with the solutions of $\mathcal{N}_\varrho$ decomposed temperature seeking sub-problems. The representative temperature points ${}_{i'}NFCM, (i' = 1, ..., L)$ are derived by comparing the fitness value $g^{tf}\left({}_{i'}\mathcal{X}\left|{}_{i'}\vec{\omega}^j, {}_{i'}r^*\right.\right)$ of aggregate function (3). In the MO-FEO algorithm, each sub-problem has one and only one different weight vector. Each optimal solution of the corresponding weight vector ${}_{i'}\vec{\omega}^j = \left({}_{i'}\omega_1^j, \cdots, {}_{i'}\omega_L^j\right)^T$ is maintained during the evolution process. The approximation optimal PF is affected by the selection pressure determined. It means that the selection of representative temperature point ${}_{i'}NFCM$ is determined by this pressure. The individual would approach gradually the temperature reference point ${}_{i'}r^*$ under the selection pressure until that it intersects with the optimal PF contained the optimal solutions for the scalar optimization problem.

Without loss of generality, take the evolution process of the $L = 3$ objective function as an example. In this situation, the weight vector is ${}_{i'}\vec{\omega}^j = \left({}_{i'}\omega_1^j, {}_{i'}\omega_2^j, {}_{i'}\omega_3^j\right)^T$ satisfying $\sum_{i=1}^{3} {}_{i'}\omega_i^j = 1$ and ${}_{i'}\omega_1^j, {}_{i'}\omega_2^j, {}_{i'}\omega_3^j \ge 0$. ${}_{i'}f\left({}_{i'}\mathcal{X}^*\right) = \left({}_{i'}f_1\left({}_{i'}\mathcal{X}^*\right), {}_{i'}f_2\left({}_{i'}\mathcal{X}^*\right), {}_{i'}f_3\left({}_{i'}\mathcal{X}^*\right)\right)$ is the pareto optimal solution corresponding to ${}_{i'}\vec{\omega}^j$. At first, consider a simple weight vector ${}_{i'}\vec{\omega}^j = (1, 0, 0)^T$. As depicted in Figure 4(a), the selection pressure in the case depends only on the objective function ${}_{i'}f_1$, that is $g^{tf}\left({}_{i'}\mathcal{X}\left|{}_{i'}\vec{\omega}^j, {}_{i'}r^*\right.\right) = \max_{1\le i\le 3}\left\{{}_{i'}\omega_i^j\left|{}_{i'}f_i\left({}_{i'}\mathcal{X}\right) - {}_{i'}r_i^*\right|\right\} = {}_{i'}\omega_1^j\left|{}_{i'}f_1\left({}_{i'}\mathcal{X}\right) - {}_{i'}r_1^*\right|$. Hence, the new solution is influenced by the selection pressure and will evolve toward the ${}_{i'}f_2 - {}_{i'}f_3$ plane (i.e. the plane constructed by the ${}_{i'}f_2$ and ${}_{i'}f_3$ axes). In Figure 4(a), the point ${}_{i'}\mathcal{X}_A$ evolves from the point ${}_{i'}\mathcal{X}$, and the point ${}_{i'}\mathcal{X}_B$ evolves from the point ${}_{i'}\mathcal{X}_A$. Hence, the evolutionary process continues until the point ${}_{i'}\mathcal{X}$ converges to ${}_{i'}\mathcal{X}^*$, then there is ${}_{i'}f_1\left({}_{i'}\mathcal{X}\right) > {}_{i'}f_1\left({}_{i'}\mathcal{X}_A\right) > {}_{i'}f_1\left({}_{i'}\mathcal{X}_B\right) > {}_{i'}f_1\left({}_{i'}\mathcal{X}^*\right) = {}_{i'}r_1^*$. After each evolution, ${}_{i'}f_1\left({}_{i'}\mathcal{X}\right)$ can draw nearer to ${}_{i'}r_1^*$, and the value of ${}_{i'}\omega_1^j\left|{}_{i'}f_1\left({}_{i'}\mathcal{X}\right) - {}_{i'}r_1^*\right|$ is getting smaller, which is: $g^{tf}\left({}_{i'}\mathcal{X}\left|{}_{i'}\vec{\omega}^j, {}_{i'}r^*\right.\right) > g^{tf}\left({}_{i'}\mathcal{X}_A\left|{}_{i'}\vec{\omega}^j, {}_{i'}r^*\right.\right) > g^{tf}\left({}_{i'}\mathcal{X}_B\left|{}_{i'}\vec{\omega}^j, {}_{i'}r^*\right.\right) > g^{tf}\left({}_{i'}\mathcal{X}^*\left|{}_{i'}\vec{\omega}^j, {}_{i'}r^*\right.\right) = 0$.

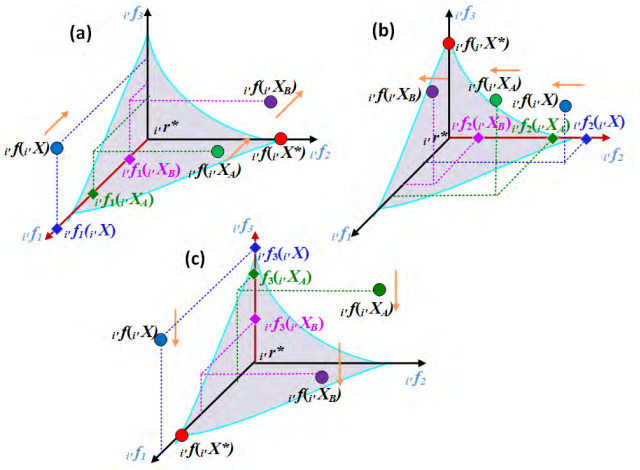

FIGURE 4. The influence of selection pressure under special weight vector during evolution.

Similarly, considering ${}_{i'}\vec{\omega}^j = (0, 1, 0)^T$, ${}_{i'}\vec{\omega}^j = (0, 0, 1)^T$, their corresponding selection pressure replies separately on ${}_{i'}f_2$ and ${}_{i'}f_3$. As shown in Figure 4(b), the new solution is influenced under the selection pressure and will evolve toward the ${}_{i'}f_1 - {}_{i'}f_3$ plane when ${}_{i'}\vec{\omega}^j = (0, 1, 0)^T$. As given in Figure 4(c), the new solution is influenced by the selection pressure and will evolve toward the ${}_{i'}f_1 - {}_{i'}f_2$ plane when ${}_{i'}\vec{\omega}^j = (0, 0, 1)^T$. Finally, they can get respectively closer to the optimal solutions ${}_{i'}r_2^*$ and ${}_{i'}r_3^*$.

Next, consider the more general case when ${}_{i'}\omega_i^j \in (0, 1), i = 1, 2, 3$. As illustrated in Figure 5, the optimal solution ${}_{i'}f\left({}_{i'}\mathcal{X}^*\right)$ denotes the intersection of the PF and the brown line where the weight vector ${}_{i'}\vec{\omega}^j$ is located. Actually, the brown line is through the PF solution $\left({}_{i'}f_1\left({}_{i'}\mathcal{X}^*\right), {}_{i'}f_2\left({}_{i'}\mathcal{X}^*\right), {}_{i'}f_3\left({}_{i'}\mathcal{X}^*\right)\right)$ and the temperature reference point ${}_{i'}r^* = \left({}_{i'}r_1^*, {}_{i'}r_2^*, {}_{i'}r_3^*\right)$, which is the selection pressure to get the front solution ${}_{i'}f\left({}_{i'}\mathcal{X}^*\right)$. The fitness value of ${}_{i'}\mathcal{X}^*$ satisfies ${}_{i'}\omega_1^j\left({}_{i'}f_1\left({}_{i'}\mathcal{X}^*\right) - {}_{i'}r_1^*\right) = {}_{i'}\omega_2^j\left({}_{i'}f_2\left({}_{i'}\mathcal{X}^*\right) - {}_{i'}r_2^*\right) = {}_{i'}\omega_3^j\left({}_{i'}f_3\left({}_{i'}\mathcal{X}^*\right) - {}_{i'}r_3^*\right)$. Moreover, each point ${}_{i'}f\left({}_{i'}\mathcal{X}\right)$ of the brown line can be satisfied $\frac{{}_{i'}f_1\left({}_{i'}\mathcal{X}\right) - {}_{i'}r_1^*}{{}_{i'}f_1\left({}_{i'}\mathcal{X}^*\right) - {}_{i'}r_1^*} = \frac{{}_{i'}f_2\left({}_{i'}\mathcal{X}\right) - {}_{i'}r_2^*}{{}_{i'}f_2\left({}_{i'}\mathcal{X}^*\right) - {}_{i'}r_2^*} = \frac{{}_{i'}f_3\left({}_{i'}\mathcal{X}\right) - {}_{i'}r_3^*}{{}_{i'}f_3\left({}_{i'}\mathcal{X}^*\right) - {}_{i'}r_3^*}$.

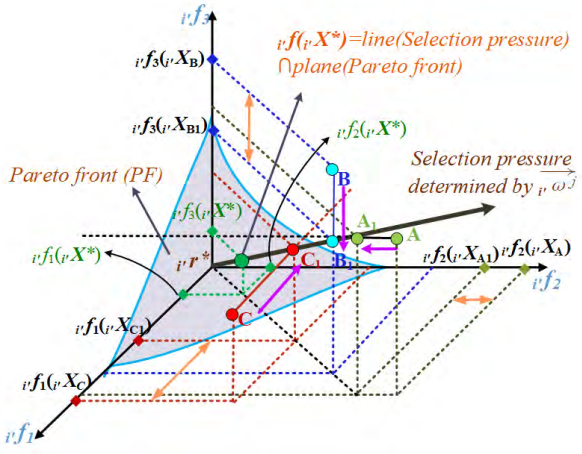

FIGURE 5. The influence of selection pressure under weight vector without zero component during evolution.

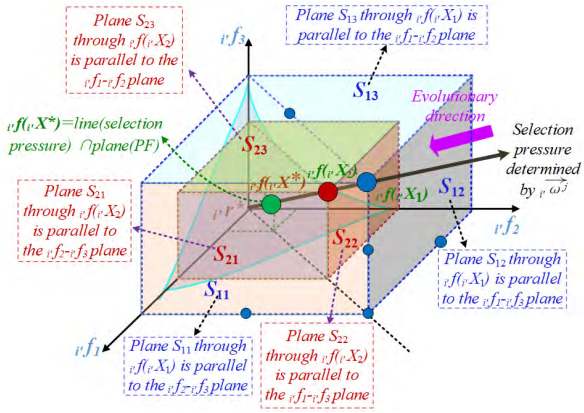

FIGURE 6. The relationship between arbitrary solutions and solutions on the selection pressure.

Hence, we can further obtain

$$\frac{{}_{i'}f_1\left({}_{i'}\mathcal{X}\right)-{}_{i'}r_1^*}{{}_{i'}f_2\left({}_{i'}\mathcal{X}\right)-{}_{i'}r_2^*}=\frac{{}_{i'}f_1\left({}_{i'}\mathcal{X}^*\right)-{}_{i'}r_1^*}{{}_{i'}f_2\left({}_{i'}\mathcal{X}^*\right)-{}_{i'}r_2^*}=\frac{{}_{i'}\omega_2^j}{{}_{i'}\omega_1^j}$$
$$\frac{{}_{i'}f_1\left({}_{i'}\mathcal{X}\right)-{}_{i'}r_1^*}{{}_{i'}f_3\left({}_{i'}\mathcal{X}\right)-{}_{i'}r_3^*}=\frac{{}_{i'}f_1\left({}_{i'}\mathcal{X}^*\right)-{}_{i'}r_1^*}{{}_{i'}f_3\left({}_{i'}\mathcal{X}^*\right)-{}_{i'}r_3^*}=\frac{{}_{i'}\omega_3^j}{{}_{i'}\omega_1^j}$$
$$\frac{{}_{i'}f_2\left({}_{i'}\mathcal{X}\right)-{}_{i'}r_2^*}{{}_{i'}f_3\left({}_{i'}\mathcal{X}\right)-{}_{i'}r_3^*}=\frac{{}_{i'}f_2\left({}_{i'}\mathcal{X}^*\right)-{}_{i'}r_2^*}{{}_{i'}f_3\left({}_{i'}\mathcal{X}^*\right)-{}_{i'}r_3^*}=\frac{{}_{i'}\omega_3^j}{{}_{i'}\omega_2^j} \quad (7)$$

Hence, ${}_{i'}\omega_1^j\left({}_{i'}f_1\left({}_{i'}\mathcal{X}\right)-{}_{i'}r_1^*\right)={}_{i'}\omega_2^j\left({}_{i'}f_2\left({}_{i'}\mathcal{X}\right)-{}_{i'}r_2^*\right)={}_{i'}\omega_3^j\left({}_{i'}f_3\left({}_{i'}\mathcal{X}\right)-{}_{i'}r_3^*\right)$.

It is clear that $g^{tf}\left({}_{i'}\mathcal{X}|\,\vec{{}_{i'}\omega^j},{}_{i'}r^*\right)=\max\limits_{1\le i\le 3}\left\{{}_{i'}\omega_i^j\left|{}_{i'}f_i\left({}_{i'}\mathcal{X}\right)-{}_{i'}r_i^*\right|\right\}>g^{tf}\left({}_{i'}\mathcal{X}^*|\,\vec{{}_{i'}\omega^j},{}_{i'}r^*\right)={}_{i'}\omega_i^j\left|{}_{i'}f_i\left({}_{i'}\mathcal{X}^*\right)-{}_{i'}r_i^*\right|$. In the evolutionary process, the evolution direction of ${}_{i'}f\left({}_{i'}\mathcal{X}\right)$ would be affected by the selection pressure under the Tchebycheff aggregation, while comparing ${}_{i'}f\left({}_{i'}\mathcal{X}\right)$ with the point of the brown line determined by $\vec{{}_{i'}\omega^j}$. As exhibited in Figure 5, the point A (that is, $\left({}_{i'}f_1\left({}_{i'}\mathcal{X}_A\right),{}_{i'}f_2\left({}_{i'}\mathcal{X}_A\right),{}_{i'}f_3\left({}_{i'}\mathcal{X}_A\right)\right)$) is in the feasible domain, and the corresponding point A_1 (i.e. $\left({}_{i'}f_1\left({}_{i'}\mathcal{X}_{A_1}\right),{}_{i'}f_2\left({}_{i'}\mathcal{X}_{A_1}\right),{}_{i'}f_3\left({}_{i'}\mathcal{X}_{A_1}\right)\right)$) is on the brown line. Based on the above illustration, ${}_{i'}\omega_1^j\left({}_{i'}f_1\left({}_{i'}\mathcal{X}_{A_1}\right)-{}_{i'}r_1^*\right)={}_{i'}\omega_2^j\left({}_{i'}f_2\left({}_{i'}\mathcal{X}_{A_1}\right)-{}_{i'}r_2^*\right)={}_{i'}\omega_3^j\left({}_{i'}f_3\left({}_{i'}\mathcal{X}_{A_1}\right)-{}_{i'}r_3^*\right)={}_{i'}\omega_1^j\left({}_{i'}f_1\left({}_{i'}\mathcal{X}_A\right)-{}_{i'}r_1^*\right)={}_{i'}\omega_3^j\left({}_{i'}f_3\left({}_{i'}\mathcal{X}_A\right)-{}_{i'}r_3^*\right)$. Furthermore, it can be derived that ${}_{i'}\omega_2^j\left({}_{i'}f_2\left({}_{i'}\mathcal{X}_A\right)-{}_{i'}r_2^*\right)>{}_{i'}\omega_1^j\left({}_{i'}f_1\left({}_{i'}\mathcal{X}_A\right)-{}_{i'}r_1^*\right)={}_{i'}\omega_3^j\left({}_{i'}f_3\left({}_{i'}\mathcal{X}_A\right)-{}_{i'}r_3^*\right)$ due to ${}_{i'}f_2\left({}_{i'}\mathcal{X}_A\right)>{}_{i'}f_2\left({}_{i'}\mathcal{X}_{A_1}\right)$. $g^{tf}\left({}_{i'}\mathcal{X}_A\left|\vec{{}_{i'}\omega^j},{}_{i'}r^*\right.\right)=\max\left\{{}_{i'}\omega_i^j\left|{}_{i'}f_i\left({}_{i'}\mathcal{X}_A\right)-{}_{i'}r_i^*\right|\right\}={}_{i'}\omega_2^j\left({}_{i'}f_2\left({}_{i'}\mathcal{X}_A\right)-{}_{i'}r_2^*\right)$ can be ensured for the point A. Hence, the new solution under the selection pressure would evolve toward the ${}_{i'}f_1-{}_{i'}f_3$ plane by reducing the ${}_{i'}f_2$ value. That is, the point A in the evolutionary process can move toward the point A_1.

Similar as the above analysis, consider the points B, C (that is, $\left({}_{i'}f_1\left({}_{i'}\mathcal{X}_B\right),{}_{i'}f_2\left({}_{i'}\mathcal{X}_B\right),{}_{i'}f_3\left({}_{i'}\mathcal{X}_B\right)\right)$, $\left({}_{i'}f_1\left({}_{i'}\mathcal{X}_C\right),{}_{i'}f_2\left({}_{i'}\mathcal{X}_C\right),{}_{i'}f_3\left({}_{i'}\mathcal{X}_C\right)\right)$) and their corresponding points B_1 (that is, $\left({}_{i'}f_1\left({}_{i'}\mathcal{X}_{B_1}\right),{}_{i'}f_2\left({}_{i'}\mathcal{X}_{B_1}\right),{}_{i'}f_3\left({}_{i'}\mathcal{X}_{B_1}\right)\right)$) and C_1 (that is, $\left({}_{i'}f_1\left({}_{i'}\mathcal{X}_{C_1}\right),{}_{i'}f_2\left({}_{i'}\mathcal{X}_{C_1}\right),{}_{i'}f_3\left({}_{i'}\mathcal{X}_{C_1}\right)\right)$) on the blown line in Figure 5. For the point B, the new solution under the selection pressure can evolve toward the ${}_{i'}f_1-{}_{i'}f_2$ plane by reducing the ${}_{i'}f_3$ value. That is, the point B in the evolutionary process moves toward the point B_1. For point C, the new solution under the selection pressure can evolve toward the ${}_{i'}f_2-{}_{i'}f_3$ plane by reducing the ${}_{i'}f_1$ value. That is, C in the evolutionary process moves toward C_1.

From the above analysis, one has ${}_{i'}\omega_1^j\left({}_{i'}f_1\left({}_{i'}\mathcal{X}_1\right)-{}_{i'}r_1^*\right)={}_{i'}\omega_2^j\left({}_{i'}f_2\left({}_{i'}\mathcal{X}_1\right)-{}_{i'}r_2^*\right)={}_{i'}\omega_3^j\left({}_{i'}f_3\left({}_{i'}\mathcal{X}_1\right)-{}_{i'}r_3^*\right)$ for any point ${}_{i'}f\left({}_{i'}\mathcal{X}_1\right)$ of the brown line determined by $\vec{{}_{i'}\omega^j}$. Furthermore, consider the three planes S_{11}, S_{12} and S_{13} through the point ${}_{i'}f\left({}_{i'}\mathcal{X}_1\right)=\left({}_{i'}f_1\left({}_{i'}\mathcal{X}_1\right),{}_{i'}f_2\left({}_{i'}\mathcal{X}_1\right),{}_{i'}f_3\left({}_{i'}\mathcal{X}_1\right)\right)$ where the planes S_{11}, S_{12} and S_{13} are separately parallel to the ${}_{i'}f_2-{}_{i'}f_3$ plane, the ${}_{i'}f_1-{}_{i'}f_3$ plane and the ${}_{i'}f_1-{}_{i'}f_2$ plane, as shown in Figure 6. Actually, one has that ${}_{i'}\omega_i^j\left({}_{i'}f_i\left({}_{i'}\mathcal{X}_{s_{1i}}\right)-{}_{i'}r_i^*\right)={}_{i'}\omega_i^j\left({}_{i'}f_i\left({}_{i'}\mathcal{X}_1\right)-{}_{i'}r_i^*\right)$ for any point $\left({}_{i'}f_1\left({}_{i'}\mathcal{X}_{s_{1i}}\right),{}_{i'}f_2\left({}_{i'}\mathcal{X}_{s_{1i}}\right),{}_{i'}f_3\left({}_{i'}\mathcal{X}_{s_{1i}}\right)\right)$ in the planes S_{1i}, $(i=1,2,3)$. Next, as shown again in the figure for the other point ${}_{i'}f\left({}_{i'}\mathcal{X}_2\right)$ of the brown line and the three planes S_{21}, S_{22} and S_{23} through ${}_{i'}f\left({}_{i'}\mathcal{X}_2\right)$ in which S_{21}, S_{22} and S_{23} are separately parallel to the ${}_{i'}f_2-{}_{i'}f_3$, ${}_{i'}f_1-{}_{i'}f_3$ and ${}_{i'}f_1-{}_{i'}f_2$ planes, one can also have ${}_{i'}\omega_i^j\left({}_{i'}f_i\left({}_{i'}\mathcal{X}_{s_{2i}}\right)-{}_{i'}r_i^*\right)={}_{i'}\omega_i^j\left({}_{i'}f_i\left({}_{i'}\mathcal{X}_2\right)-{}_{i'}r_i^*\right)$ for any point ${}_{i'}f_i\left({}_{i'}\mathcal{X}_{s_{2i}}\right)$ in the plane S_{2i}, $(i=1,2,3)$. For the points in the planes S_{1i}, $(i=1,2,3)$, their fitness values are same as the fitness value of ${}_{i'}f\left({}_{i'}\mathcal{X}_1\right)$. Hence, the solutions in the planes S_{1i} that are not on the brown line can be projected onto the selection pressure. Similarly, the fitness values of the points in the plane S_{2i}, $(i=1,2,3)$ are equal to the fitness value of ${}_{i'}f\left({}_{i'}\mathcal{X}_2\right)$. The solutions in the planes S_{2i} that are not on the brown line can be also projected onto the selection pressure. Thus, the relationship between good and bad solutions in space can be analyzed and discussed by comparing the fitness values on the selection pressure,

to realize the selection of representative temperature point ${}_{i'}NFCM$. The tchebycheff decomposition strategy can always try to minimize the fitness values in evolutionary process, to draw the solution to the optimal value along with the evolutionary direction $\left(1/{}_{i'}\omega_1^j, 1/{}_{i'}\omega_2^j, 1/{}_{i'}\omega_3^j\right)^T$, as depicted in Figure 6.

Considering the general situation (i.e. not only considering $L = 3$), one can derive $\frac{{}_{i'}f_1({}_{i'}\mathcal{X})-{}_{i'}r_1^*}{\frac{1}{{}_{i'}\omega_1^j}} = \frac{{}_{i'}f_2({}_{i'}\mathcal{X})-{}_{i'}r_2^*}{\frac{1}{{}_{i'}\omega_2^j}} = \cdots = \frac{{}_{i'}f_L({}_{i'}\mathcal{X})-{}_{i'}r_L^*}{\frac{1}{{}_{i'}\omega_L^j}}$ for any point ${}_{i'}f({}_{i'}\mathcal{X})$ on the selection pressure. It is worth mentioning that the selection pressure denotes a line across the point ${}_{i'}r^* = \left({}_{i'}r_1^*, {}_{i'}r_2^*, \cdots, {}_{i'}r_L^*\right)^T$ with the slope $\left(\frac{1}{{}_{i'}\omega_1^j}, \frac{1}{{}_{i'}\omega_2^j}, \cdots, \frac{1}{{}_{i'}\omega_L^j}\right)$, when the weight vector is $\left(\frac{1}{{}_{i'}\omega_1^j}, \frac{1}{{}_{i'}\omega_2^j}, \cdots, \frac{1}{{}_{i'}\omega_L^j}\right)$. When optimizing the solution in the L-dimensional target space, the pressure direction will drive ${}_{i'}f({}_{i'}\mathcal{X})$ along the evolutionary direction $\left(\frac{1}{{}_{i'}\omega_1^j}, \frac{1}{{}_{i'}\omega_2^j}, \cdots, \frac{1}{{}_{i'}\omega_L^j}\right)$, to seek for the point ${}_{i'}f({}_{i'}\mathcal{X}^*)$ on the PF.

Besides of the proposed MO-FEO scheme, the following section will further develop a whole damage evaluation method that contains variable step search and classification of temperature points, in order to evaluate quantificationally the HVI damages and enhance the efficiency of M/OD impact risks assessment.

III. DAMAGE EVALUATION METHOD WITH THE PROPOSED MO-FEO ALGORITHM

In the evaluation of the M/OD impact damages, the damages change the temperature distribution in the part zones. In this section, a damage evaluation method with the proposed MO-FEO algorithm will be developed to evaluate quantificationally the M/OD impact damages.

First of all, the definitions are introduced as follows: M and N express separately the total number of rows and columns in 3 dimensional ($3d$) matrix D. T represents the total number of the images in the time axis t. L indicates the number of classifications. The Pearson Correlation Coefficient is presented as PCC. The proposed method is exhibited follows:

Step 1: D records the initial thermal images. $D(\gamma, c, :)$ denotes the vector in the γ-th row and c-th column of D, which represents TTR. Its third-dimension expresses the time axis t. Seek the maximum temperature value $D(R_{mm}, C_{mm}, T_{mm}) = \max_{\substack{\gamma=1,2,\cdots,M \\ c=1,2,\cdots,N \\ t=1,2,\cdots,T}} [D(\gamma, c, t)]$. Define temperature thresholds $T_C(k)$, $(k = 1, 2, \cdots, K-1)$. From these thresholds, the row involving $D(R_{mm}, C_{mm}, T_{mm})$ could be split to K data-blocks marked as "Block C_k",$(k = 1, 2, \cdots, K)$, to count the length of the interval in the vertical axis. Furthermore, seek the maximum temperature value $D^k(R_{mm}, C_m^k, :)$ in "Block C_k"$(k = 1, 2, \cdots, K)$ and define its temperature threshold $THRE_{CL^k}$. Then, calculate respectively $PCC(D^k(R_{mm}, C_m^k, :), D^k(R_{mm}, c, :))$, $c = (1, 2, \cdots, C_m^k - 1)$ and $c = (C_m^k + 1, C_m^k + 2, \cdots, len_k^C)$ until their $PCC \le THRE_{CL^k}$, where PCC represents the pearson correlation coefficient, $D^k(R_{mm}, c, :)$ is the c-th vector and len_k^C denotes the number of TTR of "Block C_k". And the corresponding number of $D^k(R_{mm}, c, :)$ satisfying $PCC > THRE_{CL^k}$ are regarded as l_{k1} and l_{k2}. Therefore the seeking-interval value in "Block C_k" is $CL^k = \max\{l_{k1}, l_{k2}\}$. Next, define temperature thresholds $T_R(h)$, $(h = 1, 2, \cdots, H-1)$. The column involving $D(R_{mm}, C_{mm}, T_{mm})$ can be split into H data-blocks marked as "Block R_h",$(h = 1, 2, \cdots, H)$, according to these thresholds. Furthermore, find the maximum temperature value $D^h(R_m^h, C_{mm}, :)$ in "Block R_h"$(h = 1, 2, \cdots, H)$ and set its temperature threshold $THRE_{RL^h}$. Calculate respectively $PCC(D^h(R_m^h, C_{mm}, :), D^h(\gamma, C_{mm}, :))$, $\gamma = (1, \cdots, R_m^h - 1)$ and $\gamma = (R_m^h + 1, R_m^h + 2, \cdots, len_h^R)$ until their $PCC \le THRE_{RL^k}$ where $D^h(\gamma, C_{mm}, :)$ is the γ-th vector and len_h^R denotes the number of TTR of "Block R_h". And the corresponding number of $D^h(\gamma, C_{mm}, :)$ satisfying $PCC > THRE_{RL^h}$ are regarded as l_{h3} and l_{h4}, therefore the seeking-interval value in "Block R_h" is $RL^h = \max\{l_{h3}, l_{h4}\}$. Then, set the threshold Ξ and initialize $h = 1, k = 1, g = 1, \gamma = 1, c = 1$. The following procedure is executed:

1.1) $D(\gamma, c, :)$ is stored to $\mathcal{X}(g, :)$. Let $\gamma = \gamma + RL^h$.

1.2) If $\gamma \le len_h^R$, calculate $PCC(D(\gamma, c, :), \mathcal{X}(g, :))$, else go to Step 1.4).

1.3) If $PCC < \Xi$, let $g = g + 1$, $\mathcal{X}(g, :) = D_k^p(\gamma, c, :)$, $\gamma = \gamma + RL^h$, and repeat Step 1.2), else $\gamma = \gamma + RL^h$, repeat Step 1.2).

1.4) If $\gamma < M$, let $g = g + 1$, $p = p + 1$, and repeat Step 1.1), else let $c = c + CL^k$.

1.5) If $c < len_k^C$, let $\gamma = 1$ and repeat Step 1.1); else go to Step 1.6).

1.6) If $c < N$, let $\gamma = 1$ and $k = k + 1$, repeat Step 1.1), else the procedure is completed.

The specific process of Step 1 is shown as Figure 7.

Step 2: The TTRs (i.e. $\mathcal{X}(i, :)$, $(i = 1, 2, \cdots, g)$) have been gotten by Step 1. Then, $\mathcal{X}(i, :)$, $(i = 1, 2, \cdots, g)$ will be divided into L parts, i.e.

2.1) Initialize the cluster center ${}_{j'}Center$, $(j' = 1, 2, \cdots, L)$. Moreover, define the iteration times ς, the weighting coefficient β, and the termination threshold ϵ.

2.2) Compute the membership function $v_{j'}(\mathcal{X}(i, :))$ and update cluster centers ${}_{j'}Center$ according to $v_{j'}(\mathcal{X}(i, :)) = \frac{d_{j'i}^{-2/(\beta-1)}}{\sum_{s=1}^{L} d_{si}^{-2/(\beta-1)}}$, ${}_{j'}Center = \frac{\sum_{i=1}^{g} [v_{j'}(\mathcal{X}(i,:))]^\beta \mathcal{X}(i,:)}{\sum_{i=1}^{g} [v_{j'}(\mathcal{X}(i,:))]^\beta}$, $i = 1, 2, \cdots, g$ and $j' = 1, 2, \cdots, L$. in which $d_{jk} = \left\|\mathcal{X}(k, :) - {}_{j'}Center\right\|$ expresses the Euclidean distance between the k^{th} TTR (i.e. $\mathcal{X}(k, :)$) and the j'^{th} cluster center (i.e. ${}_{j'}Center$). $v_{j'}(\mathcal{X}(i, :))$ indicates the degree of the i^{th} TTR attach to the j'^{th} cluster.

2.3) If $\left\|J_f(\varsigma) - J_f(\varsigma - 1)\right\| \ge \epsilon$, and $i < g$, $i = i + 1$, go back to Step 2.2). If $i > g$ and $j < L$, $j = j + 1$, return to Step 2.2). If $j' \ge L$, the process is finished. If $\left\|J_f(\varsigma) - J_f(\varsigma - 1)\right\| < \epsilon$, the process is finished too.

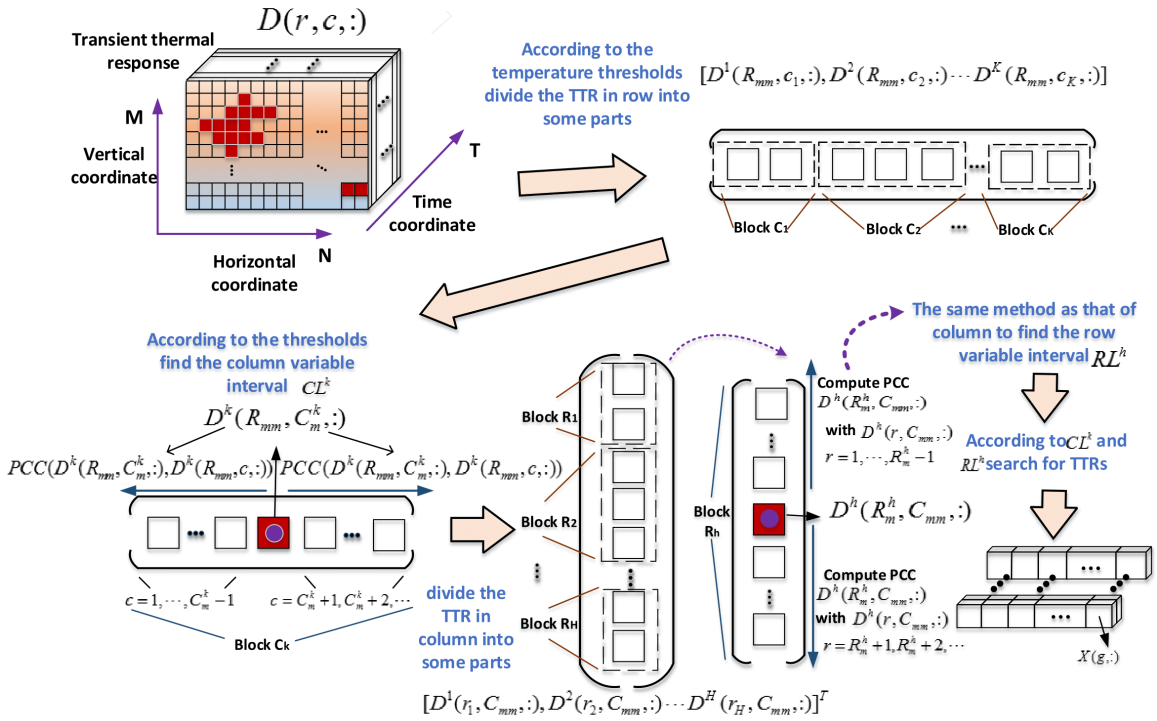

FIGURE 7. The Specific process in Step 1.

2.4) The membership maximization criterion is applied to partition $\mathcal{X}(i,:),(i = 1,2,\cdots,g)$ into L cluster ${}_{j'}\Theta$, $(j' = 1,2,\cdots,L)$.

Step 3: To find further the target damage feature information, the proposed MO-FEO algorithm is adopted to select the representative temperature point ${}_{j'}NFCM$ in each category ${}_{j'}\Omega$, $(j' = 1,2,\cdots,L)$, which is presented in Section II.

Step 4: The matrix D is transformed into $2d$ matrix U. The elements in one row of U are taken columnwise from $D(:,:,t), t = 1,2,\cdots,T$. Compute the pesudo-inverse matrix $\hat{Y}$ of Y extracted in Section II, in which $Y(:,i')$ recording the optimal solutions ${}_{i'}NFCM, (i' \in (1,2,...,L))$ derived in Step 3. Then, calculate the linear transformation $S = \hat{Y} * U$, where S represents the result of the proposed damage evaluation method, which involves the features of the thermal images processed by the proposed damage evaluation method. Moreover, continue to achieve Feature extraction of matrix using PCNN algorithm [30], which can show the defect feature from the image.

To realize the automatic recognition of HVI damage, a defect feature extraction method with the proposed MO-FEO scheme is developed in the infrared thermal wave image detection technology. Specially, the infrared imaging system record the thermal image sequence of the M/OD HVI damages. Then the presented algorithm separates the TTRs into some parts by the thresholds and seeks out the TTRs by variable interval search, which is employed to reduce the double counting of thermal characterization and keep the main feature of the M/OD HVI damages. Next, the acquired TTRs are classified by membership maximization criterion. Moreover, the proposed MO-FEO algorithm in Section II is applied to select the representative temperature points (i.e. the typical TTRs), when considering multi-performance of difference and correlation. Finally, the representative temperature points can be transformed to two-dimension matrix linearly. The typical and representative features of infrared image sequence in the M/OD impact damages can be extracted by the representative temperature points. In the following, the real infrared images data collected from two different materials with typical damages will be processed to show the effectiveness and advantages of the proposed method.

IV. EXPERIMENTAL RESULTS

In the section, two experimental cases including the comparison analysis are given to verify the validity of the proposed damage evaluation method with the MO-FEO scheme.

Case I: In this case, the thermal protection materials made of carbide and boride have been used for M/OD HVI tests on a hypervelocity ballistic range of China Aerodynamics Research and Development Center (CARDC), as depicted in Figure 8. There are four major components in HVI experimental device: (1) a two-stage light-gas gun (LGG) as the hypervelocity launcher; (2)the impact chamber within test articles; (3) the laser-photodetector speed detectors;

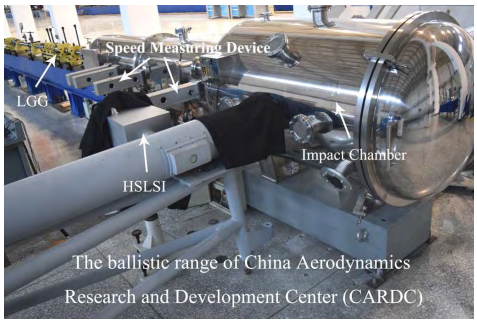

FIGURE 8. Setup for the hypervelocity impact experiment.

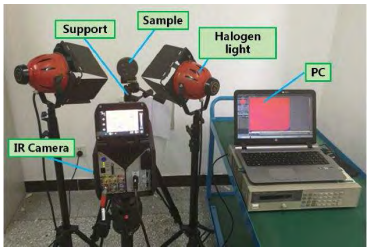

FIGURE 9. Experimental set-up for the thermal protection materials with impact damages.

and (4) Hypervelocity Sequence Laser Shadowgraph Imager (HSLSI) as the HVI process monitor. The aluminum alloy projectiles with diameter 3 mm are launched by LGG, the impact velocity is range from 1.5 km/s to 5 km/s.

After these HVI tests, the specimen with some HVI damages is thermally excited by two halogen lights and the surface temperature field change is recorded by the infrared camera with a resolution of 512 × 640. Figure 9 shows the fundamental structure of the experimental setup for the thermal image testing of the thermal protection materials with HVI damages. A total of $T = 336$ frames of thermal image sequences are captured for the thermal protection materials. Then, the proposed method is used to extract related damage features from 327680 temperature points.

The temperature thresholds are firstly set as $T_C(1) = T_R(1) = 26.8$, $T_C(2) = T_R(2) = 28.2$, respectively. The step thresholds for column are separately defined as $THRE_{CL^1} = 0.98$, $THRE_{CL^2} = 0.96$ and $THRE_{CL^3} = 0.94$. The step thresholds for row are separately selected as $THRE_{RL^1} = 0.98$, $THRE_{RL^2} = 0.96$ and $THRE_{RL^3} = 0.94$. Then, one can obtain the 478 typical temperature points (TTRs) from the original 327680 temperature points. In Step 2, let $\varsigma = 200$, $\beta = 1$, $L = 2$, $\epsilon = 10^{-5}$. Then, the total TTRs are clustered into two categories "Category A (i.e. ${}_A\Theta$) and Category B (i.e. ${}_B\Theta$)". After Step 2 of Section III, there are 237 and 241 in ${}_A\Theta$ and ${}_B\Theta$. Their corresponding cluster centers are ${}_ACenter$ and ${}_BCenter$. Figure 10 shows the clustering result including both categories of TTRs and their cluster centers, where each TTR is mapped to 3 low dimension by using the PCA algorithm [31]. It shows a good classification performance. Next, the proposed MO-FEO algorithm is applied to

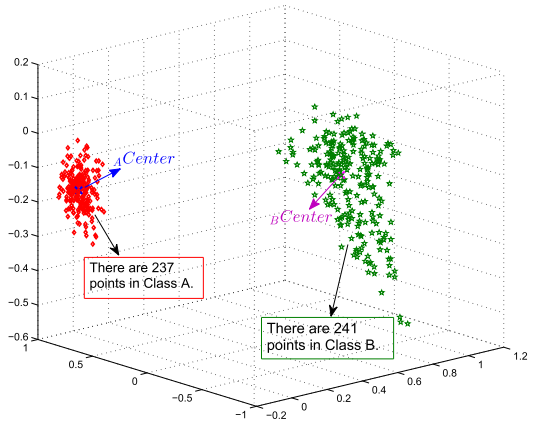

FIGURE 10. Clustering results after PCA dimensionality reduction.

select representative temperature points for Category A and Category B. Therefore, the multi-objective functions for both categories of TTRs are destabilized as follows:

For Category A:

$$\begin{aligned}
&\underset{{}_A\mathcal{X}\in{}_A\Theta}{minimize}\\
&{}_AF\left({}_A\mathcal{X}\right) = \left({}_Af_1\left({}_A\mathcal{X}\right), {}_Af_2\left({}_A\mathcal{X}\right)\right)^T,\\
&{}_Af_1\left({}_A\mathcal{X}\right) = \sqrt{\sum_{\rho=1}^{336}\left({}_Ax_h - {}_ACenter_h\right)^2}, \quad {}_A\mathcal{X}\in{}_A\Theta,\\
&{}_Af_2\left({}_A\mathcal{X}\right) = -\sqrt{\sum_{\rho=1}^{336}\left({}_Ax_h - {}_BCenter_h\right)^2}, \quad {}_A\mathcal{X}\in{}_A\Theta.
\end{aligned}$$

For Category B:

$$\begin{aligned}
&\underset{{}_B\mathcal{X}\in{}_B\Theta}{minimize}\\
&{}_BF\left({}_B\mathcal{X}\right) = \left({}_Bf_1\left({}_B\mathcal{X}\right), {}_Bf_2\left({}_BX\right)\right)^T,\\
&{}_Bf_1\left({}_B\mathcal{X}\right) = \sqrt{\sum_{\rho=1}^{336}\left({}_Bx_h - {}_BCenter_h\right)^2}, \quad {}_B\mathcal{X}\in{}_B\Theta,\\
&{}_Bf_2\left({}_B\mathcal{X}\right) = -\sqrt{\sum_{\rho=1}^{336}\left({}_Bx_h - {}_ACenter_h\right)^2}, \quad {}_B\mathcal{X}\in{}_B\Theta,
\end{aligned}$$

where ${}_ACenter = ({}_ACenter_1, \cdots, {}_ACenter_{336})$, ${}_A\mathcal{X} = ({}_Ax_1, \cdots, {}_Ax_{336}) \in {}_A\Theta$, ${}_BCenter = ({}_BCenter_1, \cdots, {}_BCenter_{336})$ and ${}_B\mathcal{X} = ({}_Bx_1, \cdots, {}_Bx_{336}) \in {}_B\Theta$. To extract the corresponding representative temperature points, we set the population number $\mathcal{N}_\varrho = 20$ and ${}_A\mathcal{GP} = {}_B\mathcal{GP} = 0.4$, and derive $\eta = \mathcal{N}_\varrho \times 15\% = 3$ in the experiment. As shown in Figures 11-12, the PF of Category A and Category B are obtained after evolutions, which have separately ${}_A\mathcal{N}_{nds} = 16$ and ${}_B\mathcal{N}_{nds} = 19$ non-dominated solutions. The number is less than 20 because some of solutions in the 20 population temperature points are dominated by solutions in the non-dominated solution set ${}_{i'}NDS$ at the time of the termination algorithm. By counting the standardized satisfaction ${}_A\mathcal{U}\left({}_A\mathcal{X}^k\right)$ and ${}_B\mathcal{U}\left({}_B\mathcal{X}^k\right)$ of the non-dominant

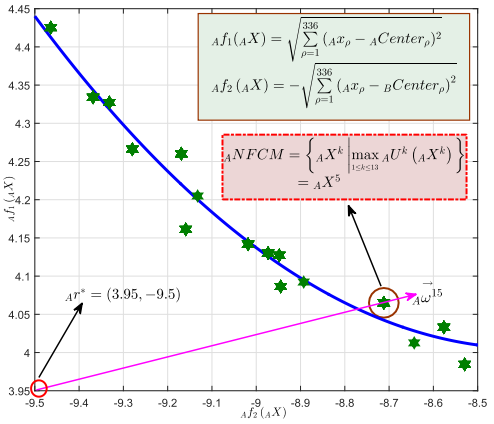

FIGURE 11. Pareto-fronts and the representative temperature point produced by the MO-FEO algorithm for Category *A*.

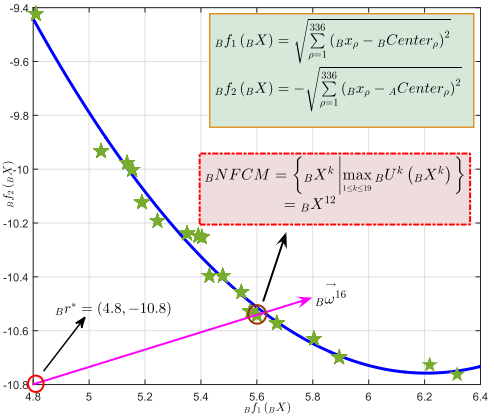

FIGURE 12. Pareto-fronts and the representative temperature point produced by the MO-FEO algorithm for Category *B*.

solutions, the relevant information of the maximum standardized satisfaction for Category A and Category B is listed in Table 3. According to $\max_{1\le k\le 16} {}_A\mathcal{U}({}_A\mathcal{X}^k) = {}_A\mathcal{U}({}_A\mathcal{X}^5) \approx 0.0892$, the compromise optimization ${}_A\mathcal{X}^5$ can be extracted as the representative temperature point of Category A by the proposed MO-FEO algorithm. Similarly, ${}_BX^{12}$ is extracted as the representative temperature point of Category B, according to $\max_{1\le k\le 19} {}_B\mathcal{U}({}_B\mathcal{X}^k) = {}_B\mathcal{U}({}_B\mathcal{X}^{12}) \approx 0.0628$. That is, the representative temperature points ${}_ANFCM = {}_A\mathcal{X}^5$, ${}_BNFCM = {}_B\mathcal{X}^{12}$ are selected in the presence of the proposed MO-FEO algorithm, as shown in Figures 11-12.

Next, a two-dimensional matrix is constructed by using ${}_ANFCM$ and ${}_BNFCM$, and two fusion images are obtained after fusion and transformation with matrix and the original infrared image, as shown in Figure 13. In the following, the maximum temperature $\mathcal{T}^{\max} = \max_{1\le i\le 336}(\mathcal{X}(i,:))$ and the rate of decline $DR = \frac{\mathcal{T}_a - \mathcal{T}_b}{\mathcal{F}_b - \mathcal{F}_c}$ will be applied to compare the representative temperature points ${}_ANFCM$ and ${}_BNFCM$, where $\mathcal{T}_a$ and $\mathcal{T}_b$ represent the temperature values of points a and b in Figure 13(c), and $\mathcal{F}_b$ and $\mathcal{F}_c$ indicate the

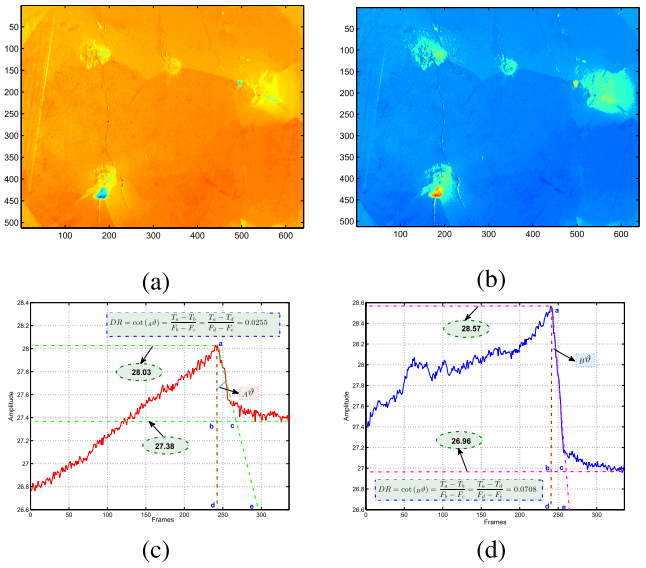

FIGURE 13. (a) Fusion image of ${}_ANFCM$. (b) Fusion image of ${}_BNFCM$. (c) Transient thermal response of ${}_ANFCM$. (d) Transient thermal response of ${}_BNFCM$.

corresponding frame values of point b and c. Moreover, one can obtain $\frac{\mathcal{T}_a - \mathcal{T}_b}{\mathcal{F}_b - \mathcal{F}_c} = \frac{\mathcal{T}_a - \mathcal{T}_d}{\mathcal{F}_d - \mathcal{F}_e}$. As shown in Figures 13(c)-(d), the maximum temperatures of ${}_ANFCM$ and ${}_BNFCM$ are $\mathcal{T}^{\max}({}_ANFCM) = 28.03$, and $\mathcal{T}^{\max}({}_BANFCM) = 28.57$. It means that ${}_BNFCM$ is heated up faster during the same heating time. Furthermore, the rate of decline of ${}_ANFCM$ and ${}_BNFCM$ are $DR({}_ANFCM) = \cot {}_A\vartheta = \frac{28.03-26.6}{282-242} = 0.0358$ and $DR({}_BNFCM) = \cot {}_B\vartheta = \frac{28.57-26.8}{267-242} = 0.0708$. One can have $DR({}_ANFCM) < DR({}_BNFCM)$. From Figure 13, the representative temperature points ${}_ANFCM$ and ${}_BNFCM$ extracted by the proposed MO-FEO algorithm can be clearly distinguished by comparing the curve of ${}_ANFCM$ and ${}_BNFCM$ including the maximum temperature and rate of decline. That is, the proposed damage evaluation method with the MO-FEO scheme has successfully selected representative temperature points of damage and background areas and extracted main damage features for M/OD HVI tests.

Next, we validate the practical performance of the proposed MO-FEO scheme for M/OD impact evaluation, in comparison with the results extracted by the difference method [19], [20] mentioned in Section II. For convenient for comparing, the man-made selection of two typical TTRs in the known test piece are denoted as two representative temperature points ${}_{Non-Dam}Point$ and ${}_{Dam}Point$ for damage and background areas. On the one hand, we use the difference method [19], [20] to select the representative temperature points ${}_ARE$ and ${}_BRE$. Table 4 shows the pearson correlation(i.e. similarity) $PCC_1({}_{Non-Dam}Point, {}_ARE)$, $PCC_2({}_{Non-Dam}Point, {}_ANFCM)$, $PCC_3({}_{Dam}Point, {}_BRE)$ and $PCC_4({}_{Dam}Point, {}_BNFCM)$. Due to $PCC_1 < PCC_2$ and $PCC_3 < PCC_4$, the representative temperature points ${}_ANFCM$ and ${}_BNFCM$ extracted by the proposed MO-FEO algorithm are more similar to the man-made selection of

TABLE 3. Relevant data when selecting the compromise optimal solution for Category *A* and *B*.

	${}_{i'}\mathcal{N}_{nds}$	Representative point	${}_{i'}\mathcal{U}\left({}_{i'}\mathcal{X}^k\right)$	${}_{i'}\mu_1\left({}_{i'}\mathcal{X}^k\right)+{}_{i'}\mu_2\left({}_{i'}\mathcal{X}^k\right)$	$\sum_{k=1}^{{}_{i'}\mathcal{N}_{nds}}\sum_{i=1}^{2}{}_{i'}\mu_i\left({}_{i'}\mathcal{X}^k\right)$
Category A	${}_{A}\mathcal{N}_{nds}=16$	${}_{A}NFCM={}_{A}\mathcal{X}^5$	0.0892	1.2741	14.2906
Category B	${}_{B}\mathcal{N}_{nds}=19$	${}_{B}NFCM={}_{B}\mathcal{X}^{12}$	0.0628	1.2007	19.1095

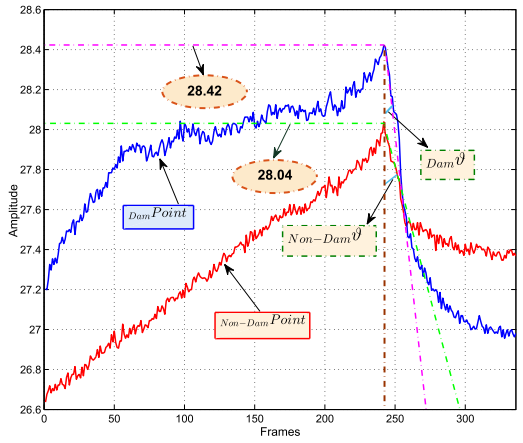

(a) The man-made selection of two typical TTRs.

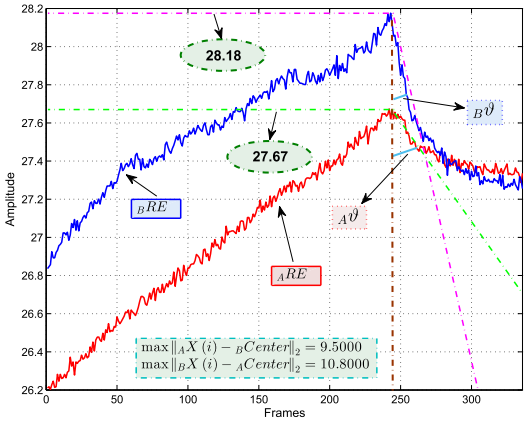

(b) The results under the difference method [19], [20].

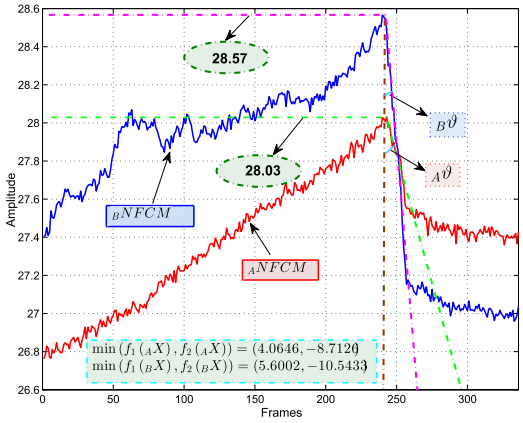

(c) The results under the proposed MO-FEO scheme.

FIGURE 14. Comparison of representative temperature points of damage and background areas.

TABLE 4. Similarity between the representative temperature points extracted by the two methods and the known points.

Representative point	Background	Damage
The difference method	$PCC_1=0.9285$	$PCC_3=0.7394$
The MO-FEO method	$PCC_2=0.9945$	$PCC_4=0.9731$

TABLE 5. Comparison of the rate of decline.

	Points	Difference	Our method
Background	$\frac{28.04-26.6}{298-242}=0.0257$	0.0097	0.0255
Damage	$\frac{28.42-26.6}{271-243}=0.0650$	0.0366	0.0703

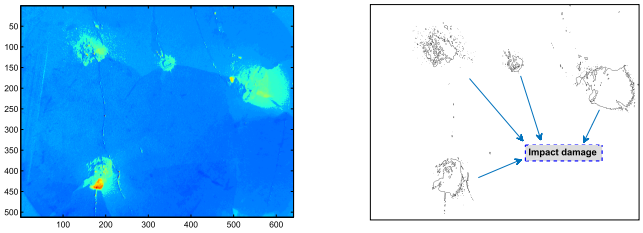

(a) (b)

FIGURE 15. (a) The image information of the damage representative point. (b) Outline damage extraction.

$_{Non-Dam}Point$ and $_{Dam}Point$, which can verify the superiority of our algorithm. Moreover, the comparison in the maximum temperature $\mathcal{T}^{\max}$ and the rate DR of decline are given to further illustrate the better performance of the proposed MO-FEO scheme. Table 5 displays separately the comparisons among DR of $_{Non-Dam}Point$, $_{A}NFCM$, $_{A}RE$, and the comparisons among DR of $_{Dam}Point$, $_{B}NFCM$, $_{B}RE$. Obviously, DR of $_{A}NFCM$ and $_{B}NFCM$ are closer to DR of $_{Non-Dam}Point$ and $_{Dam}Point$. Considering the maximum temperature aspects in Figure 21, $\mathcal{T}^{\max}$ of $_{A}NFCM$ and $_{B}NFCM$ are more similar to $\mathcal{T}^{\max}$ of $_{Non-Dam}Point$ and $_{Dam}Point$, when comparing with $\mathcal{T}^{\max}$ of $_{A}RE$ and $_{B}RE$. Then, the proposed MO-FEO algorithm can have a better performance of selecting the representative temperature point, to accurately evaluate the M/OD impact damages. Moreover, the PCNN method [30] in Step 4 is applied to build a feedback network composed by 327680 pixels of damage image. Then, the damage outline of the test piece is extracted in Figure 15. It shows that the extraction of damage features is realized to verify the validity of the proposed algorithm.

Remark 2: In addition to the typical impact craters on inorganic nonmetallic materials for the thermal protection system of reentry aircraft, there are some other HVI damages

FIGURE 16. Alloy-steel plate with artificial through-hole damage and stuffed-hole damage.

on thin-wall structure parts, such as perforation holes and intrusion objects, which are quite common in on-orbit spacecraft. Various metals like aluminum, steel, copper, titanium, magnesium and so on are often used as aerospace structural material. Hence, the simulated typical metallic material with some similar HIV damages is also designed later in this research.

Case II: In this case, an alloy-steel plate with artificial through-hole damage and stuffed-hole damage shown in Figure 16 is prepared to simulate the typical M/OD HVI damages of the usual aerospace structural metallic materials, and the evaluation experiments are carried out to demonstrate the availability and applicability of this novel damage evaluation method. A total of $T = 240$ frames of thermal image sequences are collected for the alloy-steel plate in the thermal wave image technique. The temperature thresholds are set as $T_C(1) = T_R(1) = 28.2$, $T_C(2) = T_R(2) = 31.2$, respectively. The step thresholds for column and row are separately defined as $THRE_{CL^1} = 0.98$, $THRE_{CL^2} = 0.96$, $THRE_{CL^3} = 0.94$, $THRE_{RL^1} = 0.98$, $THRE_{RL^2} = 0.96$ and $THRE_{RL^3} = 0.94$. Then, one can obtain the 290 typical temperature points (TTRs) from the original 327680 temperature points.

In Step 2, let $\varsigma = 200$, $\beta = 1$, $L = 3$, $\epsilon = 10^{-5}$. Then, the total TTRs are clustered into three categories "Category A (i.e. ${}_A\Theta$), Category B (i.e. ${}_B\Theta$) and Category C (i.e. ${}_C\Theta$)". After Step 2, there are 229, 237 and 242 in ${}_A\Theta$, ${}_B\Theta$ and ${}_C\Theta$. Their corresponding cluster centers are ${}_A Center$, ${}_B Center$ and ${}_C Center$. Figure 17 displays the clustering result involving three categories of TTRs and their cluster centers, where each TTR is mapped to 3 low dimension by utilizing the PCA algorithm [31]. It shows a good classification performance. Next, the proposed MO-FEO algorithm is employed to select representative temperature points for Category A, Category B and Category C. Therefore, the multi-objective functions for the three categories of TTRs are established as follows:

For Category A:

$$\underset{{}_A\mathcal{X}\in{}_A\Theta}{minimize}\ {}_AF\left({}_A\mathcal{X}\right) = \left({}_Af_1\left({}_A\mathcal{X}\right), {}_Af_2\left({}_A\mathcal{X}\right), {}_Af_3\left({}_A\mathcal{X}\right)\right)^T,$$

$${}_Af_1\left({}_A\mathcal{X}\right) = \sqrt{\sum_{\rho=1}^{240}\left({}_Ax_\rho - {}_ACenter_\rho\right)^2}, \quad {}_A\mathcal{X}\in{}_A\Theta,$$

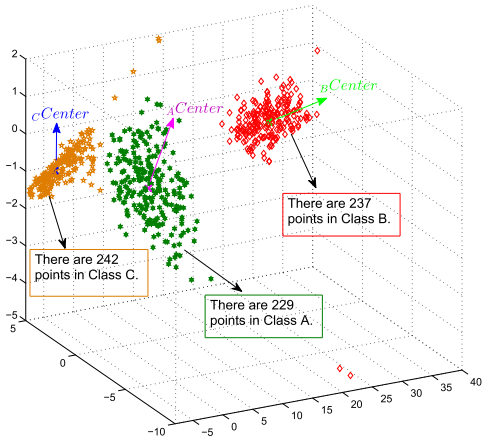

FIGURE 17. Clustering results after PCA dimensionality reduction.

$${}_Af_2\left({}_A\mathcal{X}\right) = -\sqrt{\sum_{\rho=1}^{240}\left({}_Ax_\rho - {}_BCenter_\rho\right)^2}, \quad {}_A\mathcal{X}\in{}_A\Theta,$$

$${}_Af_3\left({}_A\mathcal{X}\right) = -\sqrt{\sum_{\rho=1}^{240}\left({}_Ax_\rho - {}_CCenter_\rho\right)^2}, \quad {}_A\mathcal{X}\in{}_A\Theta.$$

For Category B:

$$\underset{{}_B\mathcal{X}\in{}_B\Theta}{minimize}\ {}_BF\left({}_B\mathcal{X}\right) = \left({}_Bf_1\left({}_B\mathcal{X}\right), {}_Bf_2\left({}_B\mathcal{X}\right), {}_Bf_3\left({}_B\mathcal{X}\right)\right)^T,$$

$${}_Bf_1\left({}_B\mathcal{X}\right) = \sqrt{\sum_{\rho=1}^{240}\left({}_Bx_\rho - {}_BCenter_\rho\right)^2}, \quad {}_B\mathcal{X}\in{}_B\Theta$$

$${}_Bf_2\left({}_B\mathcal{X}\right) = -\sqrt{\sum_{\rho=1}^{240}\left({}_Bx_\rho - {}_ACenter_\rho\right)^2}, \quad {}_B\mathcal{X}\in{}_B\Theta$$

$${}_Bf_3\left({}_B\mathcal{X}\right) = -\sqrt{\sum_{\rho=1}^{240}\left({}_Bx_\rho - {}_CCenter_\rho\right)^2}, \quad {}_B\mathcal{X}\in{}_B\Theta.$$

For Category C:

$$\underset{{}_C\mathcal{X}\in{}_C\Theta}{minimize}\ {}_CF\left({}_C\mathcal{X}\right) = \left({}_Cf_1\left({}_C\mathcal{X}\right), {}_Cf_2\left({}_C\mathcal{X}\right), {}_Cf_3\left({}_C\mathcal{X}\right)\right)^T,$$

$${}_Cf_1\left({}_C\mathcal{X}\right) = \sqrt{\sum_{\rho=1}^{240}\left({}_Cx_\rho - {}_CCenter_\rho\right)^2}, \quad {}_C\mathcal{X}\in{}_C\Theta,$$

$${}_Cf_2\left({}_C\mathcal{X}\right) = -\sqrt{\sum_{\rho=1}^{240}\left({}_Cx_\rho - {}_ACenter_\rho\right)^2}, \quad {}_C\mathcal{X}\in{}_C\Theta,$$

$${}_Cf_3\left({}_C\mathcal{X}\right) = -\sqrt{\sum_{\rho=1}^{240}\left({}_Cx_\rho - {}_BCenter_\rho\right)^2}, \quad {}_C\mathcal{X}\in{}_C\Theta,$$

where ${}_ACenter = \left({}_ACenter_1, \cdots, {}_ACenter_{240}\right)$, ${}_A\mathcal{X} = \left({}_Ax_1, \cdots, {}_Ax_{240}\right) \in {}_A\Theta$, ${}_BCenter = \left({}_BCenter_1, \cdots, {}_BCenter_{240}\right)$, ${}_BX = \left({}_Bx_1, \cdots, {}_Bx_{240}\right) \in {}_B\Theta$, ${}_CCenter = \left({}_CCenter_1, \cdots, {}_CCenter_{240}\right)$ and ${}_C\mathcal{X} = \left({}_Cx_1, \cdots,\right.$

TABLE 6. Relevant data when selecting the compromise optimal solution for Category *A*, *B* and *C*.

	${}_{i'}\mathcal{N}_{nds}$	Representative point	${}_{i'}\mathcal{U}\left({}_{i'}\mathcal{X}^k\right)$	$\sum_{i=1}^{3} {}_{i'}\mu_i\left({}_{i'}\mathcal{X}^k\right)$	$\sum_{k=1}^{{}_{i'}N_{nds}}\sum_{i=1}^{3} {}_{i'}\mu_i\left({}_{i'}\mathcal{X}^k\right)$
Category A	${}_{A}\mathcal{N}_{nds}=29$	${}_{A}NFCM={}_{A}\mathcal{X}^6$	0.0419	1.9185	45.7839
Category B	${}_{B}\mathcal{N}_{nds}=28$	${}_{B}NFCM={}_{B}\mathcal{X}^{25}$	0.0511	2.0000	39.1746
Category C	${}_{C}\mathcal{N}_{nds}=15$	${}_{C}NFCM={}_{C}\mathcal{X}^{15}$	0.1113	2.0000	17.9646

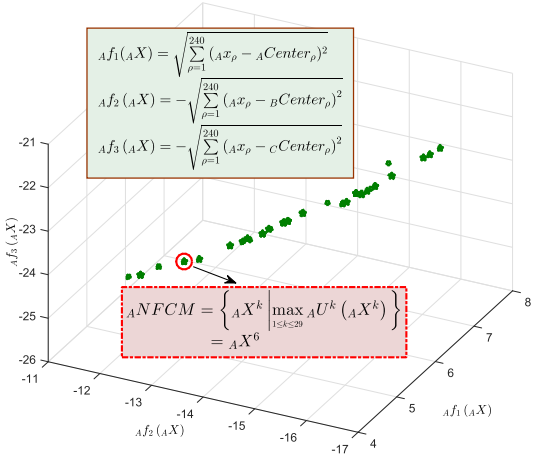

FIGURE 18. Pareto-fronts and the representative temperature point produced by the MO-FEO algorithm for Category *A*.

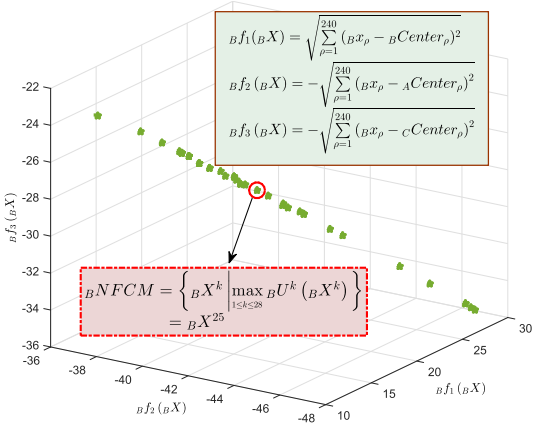

FIGURE 19. Pareto-fronts and the representative temperature point produced by the MO-FEO algorithm for Category *B*.

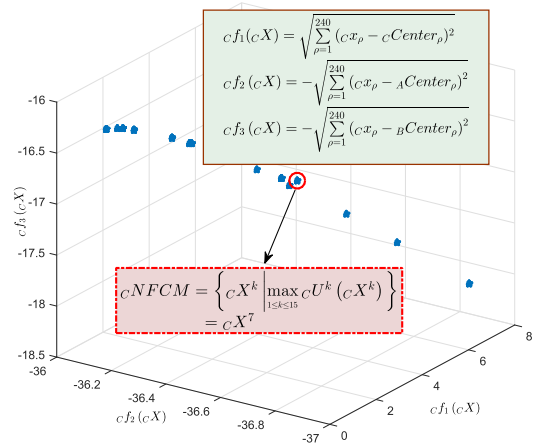

FIGURE 20. Pareto-fronts and the representative temperature point produced by the MO-FEO algorithm for Category *C*.

TABLE 7. Similarity between the representative temperature points extracted by the two methods and the known points.

Representative point	The difference method	MO-FEO method
Background	$PCC_1=0.8698$	$PCC_2=0.9986$
Damage1	$PCC_3=0.8231$	$PCC_4=0.9970$
Damage2	$PCC_5=0.9840$	$PCC_6=0.9968$

TABLE 8. Comparison of the rate of decline.

	Points	**Difference**	**MO-FEO method**
Background	0.0035	0.0083	0.0039
Damage1	0.0411	0.0267	0.0456
Damage2	0.0023	0.0012	0.0029

${}_{C}x_{240})\in{}_{C}\Theta$. We set $\mathcal{N}_{\mathcal{Q}}=30$ and ${}_{A}\mathcal{GP}={}_{B}\mathcal{GP}={}_{C}\mathcal{GP}=0.4$, and derive $\eta=\mathcal{N}_{\mathcal{Q}}\times 10\%=3$, and the variation threshold in the experiment. As depicted in Figures 18-20, the PF of Category *A*, *B* and *C* are obtained after evolutions, which have ${}_{A}\mathcal{N}_{nds}=29$, ${}_{B}\mathcal{N}_{nds}=28$ and ${}_{C}\mathcal{N}_{nds}=15$ non-dominated solutions, respectively. Then, the standardized satisfaction ${}_{A}\mathcal{U}\left({}_{A}\mathcal{X}^k\right)$, ${}_{B}U\left({}_{B}\mathcal{X}^k\right)$ and ${}_{C}\mathcal{U}\left({}_{C}\mathcal{X}^k\right)$ of these non-dominant solutions are calculated. Table 6 shows the relevant information of the maximum standardized satisfaction for Category *A*, Category *B* and Category *C*. From $\max_{1\le k\le 29}{}_{A}\mathcal{U}\left({}_{A}\mathcal{X}^k\right)={}_{A}\mathcal{U}\left({}_{A}\mathcal{X}^6\right)\approx 0.0419$, $\max_{1\le k\le 28}{}_{B}\mathcal{U}\left({}_{B}\mathcal{X}^k\right)={}_{B}\mathcal{U}\left({}_{B}\mathcal{X}^{25}\right)\approx 0.0511$ and $\max_{1\le k\le 15}{}_{C}\mathcal{U}\left({}_{C}\mathcal{X}^k\right)={}_{C}\mathcal{U}\left({}_{C}\mathcal{X}^7\right)\approx 0.1113$, the representative temperature points ${}_{A}NFCM={}_{A}\mathcal{X}^6$, ${}_{B}NFCM={}_{B}\mathcal{X}^{28}$ and ${}_{C}NFCM={}_{C}\mathcal{X}^7$ are selected by the proposed MO-FEO algorithm of Section II, as shown in Figures 18-20.

Next, a 3d matrix is constructed by using ${}_{A}NFCM$, ${}_{B}NFCM$ and ${}_{C}NFCM$, and three fusion images are obtained after fusion and transformation with matrix and the original infrared image. In the following, $\mathcal{T}^{\max}=\max_{1\le i\le 240}(\mathcal{X}(i,:))$ and $DR=\frac{\mathcal{T}_a-\mathcal{T}_b}{\mathcal{T}_b-\mathcal{T}_c}$ will be applied to compare the representative temperature points ${}_{A}NFCM$, ${}_{B}NFCM$ and ${}_{C}NFCM$. Similar to the analysis in Case 1, we study the better performance of the MO-FEO scheme for the simulated typical aerospace structural metallic material, in comparison with

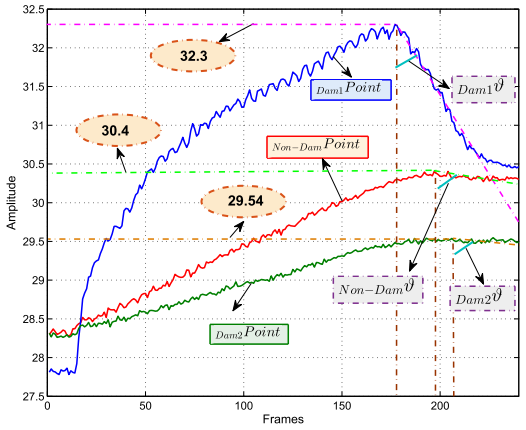

(a) The man-made selection of three typical TTRs.

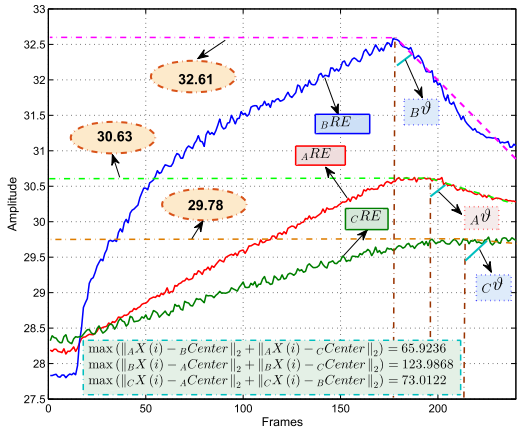

(b) The results under the difference method [19], [20].

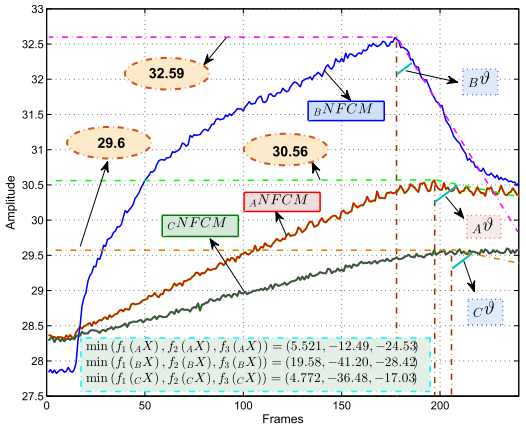

(c) The results under the MO-FEO scheme.

FIGURE 21. Comparison of representative temperature points of through-hole damage, stuffed-hole damage and background areas.

the results extracted by the difference method [19], [20]. In the known test piece, the man-made selection of three typical TTRs in advance are denoted as three representative temperature points $_{Non-Dam}Point$, $_{Dam1}Point$ and $_{Dam2}Point$ for background areas, through-hole damage and stuffed-hole damage. On the one hand, we use the difference method [19], [20] to select the representative temperature points $_{A}RE$, $_{B}RE$ and $_{C}RE$. Table 7 shows the pearson

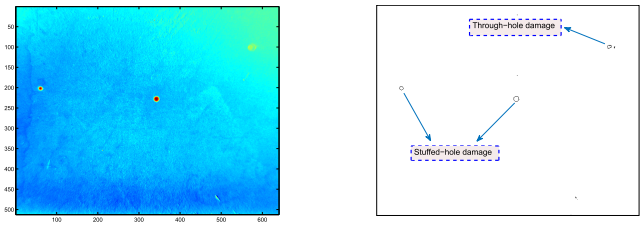

(a) (b)

FIGURE 22. (a) The image information of the damage representative point. (b) Outline damage extraction of test piece.

correlation (i.e. similarity) $PCC_1(_{Non-Dam}Point, _{A}RE)$, $PCC_2(_{Non-Dam}Point, _{A}NFCM)$, $PCC_3(_{Dam1}Point, _{B}RE)$, $PCC_4(_{Dam1}Point, _{B}NFCM)$, $PCC_5(_{Dam2}Point, _{C}RE)$ and $PCC_6(_{Dam2}Point, _{C}NFCM)$. Due to $PCC_1 < PCC_2$, $PCC_3 < PCC_4$ and $PCC_5 < PCC_6$, the representative temperature points $_{A}NFCM$, $_{B}NFCM$ and $_{C}NFCM$ extracted by the proposed MO-FEO algorithm are more similar to the man-made selection of $_{Non-Dam}Point$, $_{Dam1}Point$ and $_{Dam2}Point$, which can verify the superiority of our algorithm. Moreover, the comparison in $\mathcal{T}^{\max}$ and DR are given to further illustrate the better performance of the proposed MO-FEO scheme. Table 5 displays separately the comparisons among DR of $_{Non-Dam}Point$, $_{A}NFCM$, $_{A}RE$, and the comparisons among DR of $_{Dam}Point$, $_{B}NFCM$, $_{B}RE$. Obviously, DR of $_{A}NFCM$, $_{B}NFCM$ and $_{C}NFCM$ are closer to DR of $_{Non-Dam}Point$, $_{Dam1}Point$ and $_{Dam2}Point$. Considering the maximum temperature in Figure 21, $\mathcal{T}^{\max}$ of $_{A}NFCM$, $_{B}NFCM$ and $_{C}NFCM$ are more similar to $\mathcal{T}^{\max}$ of $_{Non-Dam}Point$, $_{Dam1}Point$ and $_{Dam2}Point$, when comparing with $\mathcal{T}^{\max}$ of $_{A}RE$, $_{B}RE$ and $_{C}RE$. Then, the proposed MO-FEO algorithm can have a better performance of selecting the representative temperature point, to accurately evaluate the M/OD impact damages. Moreover, the PCNN algorithm [31] is applied to build a feedback network composed by 327680 pixels of damage image. The damage outline of the test piece is extracted in Figure 22. It shows that the extraction of damage features is realized to verify the validity of the proposed algorithm.

V. CONCLUSION

In the paper, a multi-objective optimization method has been introduced into the infrared thermal image feature extraction, so both the differences and similarities have been considered in the selection of representative temperature points simultaneously. The Tchebycheff aggregation function has been adopted to transform the multi-objective optimization problem into several temperature seeking sub-problems. Under the influence of the selection pressure, the optimal representative temperature points of damage feature regions have been selected successfully. Besides the multi-objective optimization frame, the damage evaluation method includes variable step search and classification of temperature has been developed to enhance the efficiency of detection. Finally, the real

infrared thermal image testing experiments including M/OD HVI and artificial test articles were carried out to validate the feasibility of the proposed damage detection method, and all of these results indicate that the newly presented algorithm is more accurate than the method based on differential selection.

REFERENCES

[1] Z. Yulin and W. Zhaokui, "Space traffic safety management and control," *IEEE Trans. Intell. Transp. Syst.*, vol. 17, no. 4, pp. 1189–1192, Apr. 2016.
[2] B. Wei and B. D. Nener, "Multi-sensor space debris tracking for space situational awareness with labeled random finite sets," *IEEE Access*, vol. 7, pp. 36991–37003, 2019.
[3] E. L. Christiansen, "Meteoroid/debris shielding," Lyndon B. Johnson Space Center, Nat. Aeronaut. Space Admin., Houston, TX, USA, Tech. Rep. TP-2003-210788, 2003.
[4] J. C. Liou and N. L. Johnson, "Risks in space from orbiting debris," *Science*, vol. 311, pp. 340–341, Jan. 2006.
[5] E. L. Christiansen, J. Arnold, and B. Corsaro, "Handbook for designing MMOD protection," NASA Johnson Space Center, NASA, Washington, DC, USA, Tech. Rep. NASA/TM-2009-214785, 2009.
[6] A. Falsone and M. Prandini, "A randomized approach to probabilistic footprint estimation of a space debris uncontrolled reentry," *IEEE Trans. Intell. Transp. Syst.*, vol. 18, no. 10, pp. 2657–2666, Feb. 2017.
[7] X. Huang, C. Yin, J. Huang, X. Wen, Z. Zhao, J. Wu, and S. Liu, "Hypervelocity impact of TiB_2-based composites as front bumpers for space shield applications" *Mater. Des.*, vol. 97, pp. 473–482, May 2016.
[8] M. V. Silnikov, I. V. Guk, A. F. Nechunaev, and N. N. Smirnov, "Numerical simulation of hypervelocity impact problem for spacecraft shielding elements," *Acta Astronautica*, vol. 150, pp. 56–62, 2018.
[9] T. Maury, P. Loubet, M. Trisolini, A. Gallice, G. Sonnemann, and C. Colombo, "Assessing the impact of space debris on orbital resource in life cycle assessment: A proposed method and case study," *Sci. Total Environ.*, vol. 667, pp. 780–791, Jun. 2019.
[10] M. Vollmer and K. P. Mollmann, *Infrared Thermal Imaging: Fundamentals, Research and Applications*. Hoboken, NJ, USA: Wiley, 2017.
[11] J. Ahmad, A. Akula, R. Mulaveesala, and H. K. Sardana, "Barker-coded thermal wave imaging for non-destructive testing and evaluation of steel material," *IEEE Sensors J.*, vol. 19, no. 2, pp. 735–742, Oct. 2019.
[12] B.-L. Jian, C.-L. Chen, M.-W. Huang, and H.-T. Yau, "Emotion-specific facial activation maps based on infrared thermal image sequences," *IEEE Access*, vol. 16, pp. 735–742, 2019.
[13] A. Foudazi, A. Mirala, and M. T. Ghasr, "Active microwave thermography for nondestructive evaluation of surface cracks in metal structures," *IEEE Trans. Instrum. Meas.*, vol. 68, no. 2, pp. 576–585, Feb. 2019.
[14] X. Maldague, A. Ziadi, and M. Klein, "Double pulse infrared thermography," *NDT E Int.*, vol. 37, no. 7, pp. 559–564, 2004.
[15] M. Ishikawa, H. Hatta, Y. Habuka, R. Fukui, and S. Utsunomiya, "Detecting deeper defects using pulse phase thermography," *Infr. Phys. Technol.*, vol. 57, pp. 42–49, Mar. 2013.
[16] L. Cheng, B. Gao, G. Y. Tian, W. L. Woo, and G. Berthiau, "Impact damage detection and identification using eddy current pulsed thermography through integration of PCA and ICA," *IEEE Sensors J.*, vol. 14, no. 5, pp. 1655–1663, Jan. 2014.
[17] Y. Cheng, C. Yin, Y. Chen, L. Bai, X. Huang, X. Zhou, and F. Yang, "ICA fusion approach based on fuzzy using in eddy current pulsed thermography," *Int. J. Appl. Electromagn. Mech.*, vol. 52, pp. 443–451, Jan. 2016.
[18] B. Gao, W. L. Woo, Y. He, and G. Y. Tian, "Unsupervised sparse pattern diagnostic of defects with inductive thermography imaging system," *IEEE Trans. Ind. Informat.*, vol. 12, no. 1, pp. 371–383, Oct. 2016.
[19] P. Zhu, C. Yin, Y. Cheng, X. Huang, J. Cao, C.-M. Vong, and P. K. Wong, "An improved feature extraction algorithm for automatic defect identification based on eddy current pulsed thermography" *Mech. Syst. Signal Process.*, vol. 113, pp. 5–21, Dec. 2018.
[20] X. Huang, C. Yin, and S. Dadras, "Adaptive rapid defect identification in ECPT based on K-means and automatic segmentation algorithm," *J. Ambient Intell. Humanized Comput.*, to be published. doi: 10.1007/s12652-017-0671-5.
[21] V. M. Arellano-Quintana, E. A. Portilla-Flores, and E. A. Merchán-Cruz, "Multi-objective design optimization of a hexa-rotor with disturbance rejection capability using an evolutionary algorithm," *IEEE Access*, vol. 6, pp. 69064–69074, 2018.
[22] X. Zhou, J. Zhou, C. Yang, and W. Gui, "Set-point tracking and multi-objective optimization-based PID control for the goethite process," *IEEE Access*, vol. 6, pp. 36683–36698, 2018.
[23] D. Zhu, F. Hu, and X. Peng, "Expansion design of interferometric aperture synthesis arrays based on multi-objective optimization," *IEEE Access*, vol. 7, pp. 16787–16794, 2019.
[24] Y. Shen and Y. Wang, "Operating point optimization of auxiliary power unit using adaptive multi-objective differential evolution algorithm," *IEEE Trans. Ind. Electron.*, vol. 64, no. 1, pp. 115–124, Aug. 2017.
[25] J. Huang, Y. Liu, M. Liu, M. Cao, and Q. Yan, "Multi-objective optimization control of distributed electric drive vehicles based on optimal torque distribution," *IEEE Access*, vol. 7, pp. 16377–16394, 2018.
[26] K. Miettinen, *Nonlinear Multiobjective Optimization*. Berlin, Germany, Springer, 2012.
[27] Q. Zhang and H. Li, "MOEA/D: A multiobjective evolutionary algorithm based on decomposition," *IEEE Trans. Evol. Comput.*, vol. 11, no. 6, pp. 712–731, Dec. 2007.
[28] D. V. Balandin and M. M. Kogan, "Pareto suboptimal controllers in multi-objective disturbance attenuation problems" *Automatica*, vol. 84, pp. 56–61, Oct. 2017.
[29] X. Ma, Q. Zhang, G. Tian, J. Yang, and Z. Zhu, "On tchebycheff decomposition approaches for multiobjective evolutionary optimization," *IEEE Trans. Evol. Comput.*, vol. 22, no. 2, pp. 226–244, May 2018.
[30] A. K. Helmy and G. S. El-Taweel, "Image segmentation scheme based on SOM–PCNN in frequency domain" *Appl. Soft Comput.*, vol. 40, pp. 405–415, Mar. 2016.
[31] N. Rajic, "Principal component thermography for flaw contrast enhancement and flaw depth characterisation in composite structures," *Compos. Struct.*, vol. 58, pp. 521–528, Dec. 2002.

CHUN YIN received the Ph.D. degree from the University of Electronic Science and Technology of China, in 2014.

She was an Exchange Ph.D. Student with the Center for Self-Organizing and Intelligent Systems, Department of Electrical and Engineering, Utah State University, Logan, UT, USA, from 2011 to 2012. She was also an Exchange Ph.D. Student with the MESA Laboratory, University of California at Merced, Merced, CA, USA, from 2012 to 2013. She has been an Associate Professor with the School of Automation Engineering, University of Electronic Science and Technology of China, since July 2014. Her research interests include multi-objective evolutionary optimization, infrared thermography testing, and hypervelocity impact engineering. She received the Overall Best Paper Award at the 2015 IEEE International Instrumentation and Measurement Technology Conference. She received the Best New Scholars Award from the University of Electronic Science and Technology of China. One of her technological achievements obtained the First Prize for Scientific and Technological Progress Awards of Sichuan Province. Seven of her papers have been listed as HOT paper by Essential Science Indicators (ESI). One of her papers has been selected as the Top 5 list of Highly Cited Research in the journal of *Mechatronics*, and one of her papers has been selected as the ScienceDirect Top 25 list of Most Download Articles.

TING XUE received the B.Sc. degree in automation from the Nanjing University of Aeronautics and Astronautics, Nanjing, China, in 2017. She is currently pursuing the M.Sc. degree in control science and control engineering with the University of Electronic Science and Technology of China, Chengdu, China. Her research interests include multi-objective evolutionary optimization, damage detection, and machine learning.

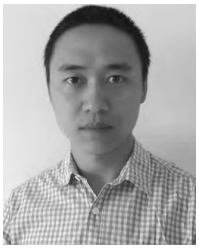

XUEGANG HUANG received the B.S. degree majoring in materials science and engineering from Southwest Jiaotong University and the M.S. and Ph.D. degrees from the Mechanical Engineering College, Shijiazhuang, China, in 2010 and 2014, respectively. His master's thesis was selected as the Excellent Master Dissertation of Hebei Province, in 2012, and his Ph.D. dissertation was selected as the National Excellent Doctoral Dissertation of China, in 2017.

He has been an Associate Researcher with the Hypervelocity Aerodynamics Institute, China Aerodynamics Research and Development Center, since 2014. His research interests include spacecraft measurement and control technology, space shielding engineering, hypervelocity impact engineering, and material dynamic behavior. He has published over 60 refereed journal articles in the above-mentioned fields.

YU-HUA CHENG received the M.S. degree from Xihua University, in 2004, and the Ph.D. degree majoring in measurement technology and industrial automation from Sichuan University, Chengdu, China, in 2007. He is currently a Professor with the University of Electronic Science and Technology of China. His research interests include industrial automation and instrumentation, damage detection technique, and fault diagnosis.

SARA DADRAS received the B.Sc. degree from Shiraz University, in 2006, and the M.Sc. and Ph.D. degrees from Tarbiat Modares University, in 2008 and 2012, respectively, all in electrical engineering.

She joined the Electrical and Computer Engineering Department, Utah State University, in 2012, as a Research Fellow. Her current research interests include hybrid electric vehicles, autonomous vehicles, renewable energy systems, image processing, and optimal controls. She is a member of ASME and SAE. She is the Organizer of the SAE Electronics Technical Committee. She currently serves as an Associate Editor for the IEEE TRANSACTIONS ON AUTOMATION SCIENCE AND ENGINEERING, IEEE ACCESS, and the *Asian Journal of Control and Complexity*.

SOODEH DADRAS received the B.Sc. degree in electrical engineering (control systems) from Shiraz University, the M.Sc. degree in electrical engineering (control systems) from Science and Research University, and the Ph.D. degree in electrical and computer engineering from Utah State University. She has worked in several other disciplines of electrical and computer engineering, particularly cyber-physical systems and mobility systems on problems at the security regarding control systems. Her research interest includes control systems, ranging from theory to design to implementation.